

Properties of Magnetohydrodynamic Normal Modes in the Earth's Magnetosphere

M.D. Hartinger^{1,2}, T. Elsdén³, M.O. Archer⁴, K. Takahashi⁵, A.N. Wright³,
A. Artemyev², X. Zhang⁶, V. Angelopoulos²

¹Space Science Institute, Colorado, USA

²Department of Earth, Planetary and Space Sciences, UCLA, California, USA

³Department of Mathematics and Statistics, University of St. Andrews, St. Andrews, UK

⁴Space and Atmospheric Physics Group, Department of Physics, Imperial College London, London, UK

⁵The Johns Hopkins University Applied Physics Laboratory, Maryland, USA

⁶University of Texas at Dallas, Texas, USA

Key Points:

- Magnetohydrodynamic normal modes are identified using ~ 13 years of observations and comparisons with numerical simulations
- Radial Alfvén speed profile peaks outside 8 Earth radii significantly alter frequencies and spatial structure of normal modes
- Frequencies and nodal structure of cavity/waveguide modes vary with magnetopause location, with power peaks well inside the magnetopause

Abstract

The Earth’s magnetosphere supports a variety of Magnetohydrodynamic (MHD) normal modes with Ultra Low Frequencies (ULF) including standing Alfvén waves and cavity/waveguide modes. Their amplitudes and frequencies depend in part on the properties of the magnetosphere (size of cavity, wave speed distribution). In this work, we use ~ 13 years of Time History of Events and Macroscale Interactions during Substorms (THEMIS) satellite magnetic field observations, combined with linearized MHD numerical simulations, to examine the properties of MHD normal modes in the region $L > 5$ and for frequencies < 80 mHz. We identify persistent normal mode structure in observed dawn sector power spectra with frequency-dependent wave power peaks like those obtained from simulation ensemble averages, where the simulations assume different radial Alfvén speed profiles and magnetopause locations. We further show with both observations and simulations how frequency-dependent wave power peaks at $L > 5$ depend on both the magnetopause location and the location of peaks in the radial Alfvén speed profile. Finally, we discuss how these results might be used to better model radiation belt electron dynamics related to ULF waves.

Plain Language Summary

The solar wind constantly disturbs plasma in the near-Earth space environment on a broad range of frequencies. However, plasma waves in the Earth’s magnetosphere, a region of space where the Earth’s magnetic field plays a dominant role in shaping plasma dynamics, often exhibit standing wave structure with a narrow range of frequencies. In other words, the magnetosphere selects standing waves with discrete frequencies from drivers with a broadband frequency spectrum. These standing waves have properties that depend on the size of the magnetosphere and plasma wave speeds. In this study, we use a database of magnetic field measurements from the Time History of Events and Macroscale Interactions during Substorms (THEMIS) satellites along with numerical simulations to isolate natural frequencies from noisy and variable driving conditions and extract standing wave spatial structure. We show how the standing wave properties change as the outer boundary of the magnetosphere and internal wave speeds change. We finally discuss how the properties of these standing waves might be used to improve space weather models.

1 Introduction

The Earth’s magnetosphere supports a wide range of plasma wave modes, with the lowest frequency waves often having spatial scales comparable to the size of the Earth’s magnetosphere. These wave frequencies correspond to the lower end of the Ultra Low Frequency (ULF) band, with frequencies $< \sim 100$ mHz. At these frequencies, wave properties and dynamics can often be modeled with a magnetohydrodynamic (MHD) approximation (e.g., Southwood & Hughes, 1983). Many observational studies have been performed on ULF waves, with early work leading to a classification scheme based on wave frequency and event duration (Jacobs et al., 1964). For example, Pc3, Pc4, and Pc5 refer to waves that last many wave cycles (“Pc” for pulsations continuous) with frequencies of ~ 22 -100 mHz, ~ 7 -22 mHz, and ~ 2 -7 mHz, respectively.

Theory, modeling, and ground-based observations of Pc3-5 waves indicate that many of these waves are related to standing MHD waves in the Earth’s magnetosphere. Sugiura and Wilson (1964) made an analogy between magnetic field lines and stretched strings to describe the dynamics of standing Alfvén waves. There are several other types of MHD waves that are partially trapped between different boundaries in the Earth’s magnetosphere, including radially trapped magnetosonic waves (e.g., reviews by Lee & Takahashi, 2006; Wright & Mann, 2006). Resonant mode conversion is also possible between standing magnetosonic waves and standing Alfvén waves via the field line resonance mechanism (Tamao, 1965; Southwood, 1974; Kivelson & Southwood, 1986).

68 These standing or partially standing waves are all generally described as normal
 69 modes, or wave modes that exist at a specific set of frequencies (f) and wavelengths (λ)
 70 for a specific set of equilibria. In the Earth’s magnetosphere, the equilibria correspond
 71 to the properties of the region the waves are confined as represented by the radial Alfvén
 72 speed profile, magnetopause location, etc. Theory and modeling both confirm that if a
 73 driving condition has a spectrum of f and λ , certain normal modes will be excited at
 74 certain frequencies (e.g., Degeling et al., 2018; Elsden & Wright, 2019). There are nu-
 75 merous examples of normal modes predicted from theory based on a box model (e.g., Kivel-
 76 son & Southwood, 1985). In the limit of zero azimuthal wave number, the Alfvén and
 77 magnetosonic modes decouple and there exists the toroidal mode (standing Alfvén wave)
 78 and cavity mode (magnetosonic mode). In the limit of large azimuthal wave number, there
 79 is only the poloidal mode standing Alfvén wave. Later modeling refinements used a wave-
 80 guide rather than a closed box geometry, leading to the development of another magne-
 81 tosonic normal mode, the waveguide mode (Samson et al., 1992). Additional model de-
 82 velopments related to wave dynamics near the plasmapause led to the concept of the vir-
 83 tual resonance (Lee & Kim, 1999); the virtual resonance model has many similarities to
 84 the cavity mode model, but due to different treatments of inner magnetosphere bound-
 85 ary conditions the two models often predict different radial amplitude structure. Still
 86 later refinements used more realistic geometries that accounted for magnetic field line
 87 curvature and flaring of the magnetopause (Wright & Elsden, 2020; Elsden & Wright,
 88 2022), compressed magnetic field and azimuthally asymmetric wave speeds (Degeling et
 89 al., 2010, 2018; Elsden et al., 2022), and local time dependent drivers (e.g., Degeling &
 90 Rankin, 2008; Elsden & Wright, 2019)

91 Observations have confirmed the existence of toroidal modes (e.g. Takahashi et al.,
 92 2015) poloidal modes (e.g., Hughes et al., 1978), cavity modes (e.g. Takahashi et al., 2010;
 93 M. Hartinger et al., 2012), waveguide modes (e.g. Mann et al., 1998), and virtual reso-
 94 nances (e.g., Shi et al., 2017) with a range of techniques based on ground-based and/or
 95 in situ measurements and in a variety of regions in the Earth’s magnetosphere. However,
 96 extracting information about normal mode properties from statistical analysis of ULF
 97 wave power is complicated by the fact that waves or transients unrelated to normal modes
 98 can contribute to wave power spectra at the frequencies of normal modes (e.g., Ander-
 99 son et al., 1990; Lessard et al., 1999; M. D. Hartinger, Angelopoulos, et al., 2013). For
 100 example, drift-mirror modes (e.g., Rae et al., 2007) and “breathing modes” (e.g., Di Mat-
 101 teo et al., 2022) can both generate large magnetic variations in the Pc5 frequency range,
 102 overlapping with the frequencies of some normal modes in the outer magnetosphere.

103 There is a strong motivation for separating MHD normal modes from other ULF
 104 waves that affect space weather when developing empirical and physics-based models of
 105 ULF wave activity. For example, MHD normal modes in the Pc4-5 frequency band (2-
 106 22 mHz) have the appropriate frequencies and phase speeds for a variety of drift and drift-
 107 bounce interactions with radiation belt and ring current electrons and ions (e.g., Elk-
 108 ington et al., 1999; Elkington & Sarris, 2016; Zong et al., 2017). ULF waves and tran-
 109 sients unrelated to normal modes can also significantly affect particle dynamics, but they
 110 do so in different ways that do not involve drift resonance. For example, drift-mirror modes
 111 with Pc5 frequencies modulate higher frequency ULF and Very Low Frequency (VLF)
 112 wave activity that in turn causes loss or acceleration (e.g., X. J. Zhang et al., 2020). Drift-
 113 mirror modes and MHD normal modes are typically combined together in statistical stud-
 114 ies of ULF wave power, and the drift-mirror modes may well be expected to dominate
 115 statistical analyses in some regions due to their large amplitudes (Zhu & Kivelson, 1991).
 116 Thus, it would be advantageous to separate them for the purpose of modeling inner mag-
 117 netosphere wave-particle interactions.

118 Statistical studies of ULF wave properties often take one of two tracks: (1) anal-
 119 ysis of band-integrated wave power/amplitude for a specific component(s) of electric or
 120 magnetic field (e.g., X. J. Zhang et al., 2020; Sandhu, Rae, Wygant, et al., 2021; Sar-

ris et al., 2022) or (2) analysis of occurrence rates of specific wave modes identified using wave polarization, spectral power peaks, etc. (e.g., Takahashi & Ukhorskiy, 2007; M. D. Hartinger, Angelopoulos, et al., 2013; Murphy et al., 2015). Despite yielding significant insight into normal mode properties and, more broadly, ULF wave properties needed for radiation belt modeling and other applications, these two approaches have some limitations when it comes to extracting the frequency and spatial dependence of normal modes from measurements. Depending on the bandwidth, the approach to analyze band-integrated wave power can average together multiple harmonics of normal modes thus obscure frequency and spatial dependence, and it cannot directly distinguish between normal modes and waves/transients unrelated to normal modes that have a broadband frequency spectrum. The approach to analyze occurrence rates is limited by a selection bias that only includes time intervals when the chosen identification criteria are satisfied, thus making it possible that some normal modes are excluded from study and making it difficult to compare occurrence rates across studies that use different selection criteria; for example, M. D. Hartinger, Angelopoulos, et al. (2013) could only obtain a lower bound occurrence rate for cavity/waveguide modes due to a sampling bias for quiet conditions when these normal modes could be uniquely identified and sorted from other activity.

Takahashi and Anderson (1992) employed a third approach to statistically characterize frequency and spatial dependent ULF wave activity. They removed background trends from wave magnetic field power spectra and organized them as a function of spatial location and the Kp index, yielding statistically representative wave magnetic field power maps as a function of frequency, local time, radial distance, magnetic latitude, and geomagnetic activity. Their approach afforded sufficient frequency resolution to resolve normal mode structure that compared favorably to numerical simulations (Lee & Lysak, 1989, 1990). However, their results only extended to a radial distance of $L \sim 6$. While there is significant observational evidence that normal modes occur at $L > 6$, it is not clear that their frequency dependent spatial structure can be identified in wave power maps using similar methods as Takahashi and Anderson (1992); there may be too much variability in the properties of normal modes in this region due to the large range of possible equilibria (wave speeds due to variable plasmasphere and ring current, range of magnetopause locations, wave frequencies, etc.), and the normal modes may be obscured by transient disturbances and other wave modes that commonly occur in this region (e.g., Zhu & Kivelson, 1991; M. D. Hartinger, Angelopoulos, et al., 2013).

In this work, we expand on earlier efforts by Takahashi and Anderson (1992) to examine normal mode spatial structure, focusing on the region $L > 6$. We compare our observational results with numerical simulations, in each case examining how normal mode properties vary for different sets of magnetospheric equilibria. Our goal is to determine (1) how normal mode properties depend on magnetospheric equilibria (magnetopause location, Alfvén speed profile) and (2) whether normal modes such as cavity/waveguide modes can be captured in statistical wave power results. In section 2, we describe the methods used for our statistical analysis of satellite magnetometer data and MHD simulations. In section 3, we show comparisons between observations and simulations for several sets of magnetospheric equilibria. In section 4, we discuss our results and their implications for radiation belt and ring current modeling. In section 5, we summarize our results.

2 Methodology

2.1 Data Analysis

2.1.1 Instrumentation

For the observational component of this study, we primarily use measurements from the fluxgate magnetometer (FGM) instrument on the five-satellite Time History of Events

171 and Macroscale Interactions during Substorms (THEMIS) mission (Auster et al., 2008;
 172 Angelopoulos, 2008). FGM data from 3 of 5 THEMIS satellites with typical apogees near
 173 12 Earth radii are used to obtain wave power spectral densities over a ~ 13 year period
 174 from 1 February 2008 to 1 December 2020; the other two satellites are less useful for this
 175 study as they entered lunar orbit in 2010. In addition to FGM, we use plasma moments
 176 from the Electrostatic Analyzer (ESA, McFadden, Carlson, Larson, Ludlam, et al., 2008)
 177 and spacecraft potential. The plasma moments are used primarily for data reduction,
 178 while spacecraft potential is used for inferring electron density to obtain information on
 179 radial Alfvén speed profile peaks. We also use geomagnetic activity indices and prop-
 180 agated solar wind measurements from NASA’s Space Physics Data Facility OMNIWeb
 181 interface hourly database. The solar wind measurements are primarily used to determine
 182 the magnetopause location using the Shue et al. (1997) model.

183 **2.1.2 Data Processing and Reduction**

184 We follow many of the data processing and data reduction steps of M. D. Hartinger,
 185 Angelopoulos, et al. (2013) and M. D. Hartinger, Moldwin, et al. (2013). The initial data
 186 processing and calibration were conducted using the open-source SPEDAS software (Angelopoulos
 187 et al., 2019) version 3.1. We follow the same procedure for each of three THEMIS space-
 188 craft: THEMIS-E, THEMIS-D, and THEMIS-A. First, we remove data when the satel-
 189 lite is in eclipse or when particle (ESA) and/or magnetic field measurements have a gap
 190 based on data products generated onboard the spacecraft. Next, magnetosheath peri-
 191 ods are identified when the satellite is at a radial distance > 8 Earth radii and one or more
 192 of the following conditions are met: electron density $> 10/cc$, perpendicular electron num-
 193 ber flux is $> 2 \times 10^7 \text{ num/cc/s}$, or velocity is $< -200 \text{ km/s}$ in the GSM x direction.
 194 We then reduce the dataset by restricting to periods when (1) the satellite is in the mag-
 195 netosphere and not the magnetosheath and (2) the satellite is at a radial distance $4.8 <$
 196 $r < 13.5 \text{ Re}$. The rationale for (1) and (2) is that we are only interested in magneto-
 197 spheric normal modes in this study, 4.8 Re is just outside the location where magnetome-
 198 ter range changes usually occur (it is usually not possible to measure small amplitude
 199 normal modes when the magnetometer is in a high range mode near perigee) and 13.5
 200 Re is close to or exceeds the maximum apogee of the THEMIS-A, D, and E satellites.
 201 Once we identify periods that meet these three criteria, we further require that they are
 202 at least 55 minutes in length to ensure a 1024 point Discrete Fourier Transform (DFT)
 203 can be conducted (51 minute DFT window plus two minutes on either side to account
 204 for magnetosheath transitions). During each of these intervals, spacecraft potential is
 205 used to infer electron density (Laakso & Pedersen, 1998; McFadden, Carlson, Larson,
 206 Bonnell, et al., 2008). The electron densities are then combined with magnetic field mea-
 207 surements from FGM to obtain the Alfvén speed by assuming a proton plasma. Dur-
 208 ing each data interval, the radial distance with maximum Alfvén speed is recorded. We
 209 refer to this as x_{ib} as in Archer et al. (2017), who associated it with the inner bound-
 210 ary of an outer magnetosphere cavity and linked it to effects on normal mode proper-
 211 ties. We also compare our x_{ib} results with those from an empirical model from Archer
 212 et al. (2017), as discussed in section 3.2.

213 Calibrated, spinfit magnetic field measurements are obtained from FGM in SM co-
 214 ordinates. The data are interpolated to have uniform 3 second time resolution, and spikes
 215 due to instrumentation artifacts are removed. Gaps in the magnetic field measurements
 216 smaller than 12 seconds are interpolated; DFT windows with larger gaps are removed
 217 from the analysis. Prior to obtaining wave power spectral densities, the magnetic field
 218 data are rotated into mean field aligned (MFA) coordinates where a single mean value
 219 for the magnetic field is obtained separately for each DFT window; as noted by Di Mat-
 220 teo and Villante (2018), this approach avoids artifacts such as artificial discrete frequency
 221 wave power peaks that would be introduced with, for example, a running mean value
 222 that changes inside the DFT window. In the MFA coordinate system, z is along the mag-
 223 netic field direction, $x = \phi_{SM} \times z$ where ϕ_{SM} is the azimuthal direction in SM coordi-

224 nates, and y completes the right hand orthogonal set. In addition to the coordinate trans-
 225 formation, we also remove slowly varying trends to better examine wave fields. For this
 226 purpose, we fit a third order polynomial to the data contained within the DFT window
 227 and subtract this polynomial from the original magnetic field measurements for the x ,
 228 y , and z components separately. Here, again, we use the same polynomial for the entirety
 229 of the 1024 point DFT window to avoid artifacts in the resulting power spectra (Di Mat-
 230 teo & Villante, 2018). Finally, wave power spectral densities are obtained. To reduce un-
 231 certainties, wave power is calculated for two DFT windows that are half the length of
 232 the broader 1024 point window, and these wave power results are averaged together. Un-
 233 certainties are further reduced by averaging over three adjacent frequency bins result-
 234 ing in the final wave power spectral density estimates. SI Figure S1 shows an example
 235 THEMIS-E satellite interval used in the database.

236 The steps above are repeated for the three THEMIS spacecraft that spend the most
 237 time in the Earth’s magnetosphere during the ~ 13 -year interval we considered: THEMIS-
 238 A, THEMIS-D, and THEMIS-E. The spacecraft sample somewhat different regions dur-
 239 ing different mission phases, though they yield similar results in the context of this study
 240 (e.g., Supporting Information Figure S2) and are combined together to form the final
 241 wave power database. This results in a database with 1984.2, 2070.9, and 2033.2 days
 242 of usable magnetic field wave power data from THEMIS-A, THEMIS-D, and THEMIS-
 243 E respectively, for a total of 6088.3 days or 171234 wave power spectra. For a single space-
 244 craft, each day corresponds to roughly 28 DFT windows that do not overlap in time, thus
 245 84 DFT windows are obtained each day when measurements from the three spacecraft
 246 are combined. Though our focus will be on wave power results from 1024 point DFT win-
 247 dows, a second database was constructed using 512 point DFT to determine whether the
 248 DFT window length significantly affected the results; as was the case for the 1024 point
 249 DFT, uncertainties in the wave power estimates are reduced by applying a three point
 250 smooth over frequency and two point average in time. No significant differences were found
 251 between the two databases, apart from the expected decrease in frequency resolution and
 252 increase in data coverage. The 1024 point DFT with three point smooth resulted in sam-
 253 ples from 0.70-160 mHz with a frequency bin spacing of 2.0 mHz whereas the 512 point
 254 DFT with three point smooth resulted in 1.3-160 mHz with a 3.9 mHz spacing. One ex-
 255 ample comparison between the 512 and 1024 point DFT results is shown in panels C and
 256 D of Figure S1, which show that results from the 512 point DFT window compare well
 257 with the 1024 point DFT window (both panels show the presence of standing Alfvén waves).
 258 Note that 1024 point DFT windows correspond to ~ 0.9 Re of spacecraft radial motion
 259 near 6 Re and $< \sim 0.1$ Re near perigee, whereas 512 point DFT windows correspond to
 260 ≤ 0.5 Re near 6 Re and $< \sim 0.05$ Re near perigee.

261 The parameters stored in the wave database include SM position of each sample
 262 (center of DFT window) and wave power for the three components of the magnetic field
 263 in MFA coordinates. The database is publicly available (Hartering, 2023).

264 **2.1.3 Statistical Analysis Methods**

265 We use median values for statistical analysis of wave power spectral density obser-
 266 vations as they are less likely to be skewed by extreme values. Figure 1A shows median
 267 wave power (units of $\frac{nT^2}{\sqrt{Hz}}$) as a function of frequency and dipole L for magnetic local
 268 times (MLT) from $6 < MLT \leq 9$ and magnetic latitudes (MLAT) > 8 degrees. In
 269 the remainder of this manuscript we focus on $6 < MLT \leq 9$ for three main reasons:
 270 (1) the radial Alfvén speed profile has somewhat less variability in this sector (Archer
 271 et al., 2015, 2017) allowing us to reduce factors we need to control for and so we can use
 272 relatively simple statistical analysis methods (i.e., median value), (2) normal modes are
 273 expected to be prevalent in this local time sector (Takahashi et al., 2015; Archer et al.,
 274 2015, 2017), and (3) for brevity, as describing the normal mode properties in all local
 275 time sectors in both simulations and data requires an extremely lengthy manuscript and

is beyond our intended scope. Note that while our wave database includes data at $r > 4.8R_E$, the L-value of the first DFT sample shown in Figure 1A starts at $> \sim 5.5$. This is primarily because of the spacecraft motion effect described at the end of section 2.1.2. A hypothetical 1024 point DFT window that began the moment an outbound spacecraft crossed $L \sim 4.8$ would have a start and stop L value of ~ 4.8 and ~ 6 . Since the spacecraft's radial velocity decreases as it moves outward, the L value at the center time of this DFT window will be closer to 6 than to 4.8.

In Figure 1A, a black dashed line is for qualitative expectations for the fundamental mode standing Alfvén wave frequency (toroidal mode) using a time of flight approximation from the Appendix of Chi and Russell (1998) that assumes a dipole magnetic field, the Carpenter and Anderson (1992) electron density model, and an assumption of an average ion mass of 1.5 amu. These calculations are used for simplicity as they are only needed for qualitative comparisons with observations needed to identify fundamental toroidal modes, but they are similar to those obtained from more sophisticated calculations based on observed electron densities and more realistic magnetic field models (e.g., Archer et al., 2015). At $L > 9$, these frequencies are also similar to observed toroidal mode frequencies by Takahashi et al. (2015) (Figure 11a in that study for the $4 < MLT < 8$ sector), while at $L < 9$ they are a ~ 2 -4 mHz higher. Note the spread in observed frequencies can be quite large, for example ranging from ~ 2 -20 mHz at $L \sim 6$ in the $4 < MLT < 8$ sector (Figure 11a of Takahashi et al. (2015)).

The most prominent feature in Figure 1A is the gradually increasing wave power with increasing radial distance at most frequencies (brighter colors at the right of the panel) and gradually decreasing wave power with increasing wave frequency (brighter colors at the bottom of the panel). These trends are consistent with past studies generally showing increased wave power at higher radial distances (e.g. X. J. Zhang et al., 2020) and lower frequencies (e.g., Takahashi & Anderson, 1992). A wave power trend following the dashed black curve for standing Alfvén waves is less clear, apart from faintly visible power enhancements seen most clearly at higher frequencies. This is no longer the case in panel B; here, robust least squares regression is used to obtain a fit between the logarithm of wave power and the logarithm of frequency for each individual DFT window using the form $\text{Log}_{10}(\text{Power}) = A * \text{Log}_{10}(\text{Frequency}) + B$ (equivalent to a power law if not in logspace). This fit to the logarithm of wave power is subtracted from the original spectra prior to taking the median value. The median wave power shown in Figure 1B thus reflects discrete frequency peaks associated with normal modes rather than background trends in power due to disturbances with more broadband frequency content (e.g., transients, drift-mirror modes). Note that Figure 1B and all subsequent wave power observations are dimensionless as subtracting the wave power trend in logspace is equivalent to obtaining the logarithm of the ratio of observed wave power to the wave power trend. Discrete frequency peaks that approximately follow the expected trend for fundamental mode standing Alfvén waves are now visible (compare dashed black curve to band of orange/yellow color) as well as higher harmonics, most likely dominated by the third and fifth harmonics (odd harmonics are expected to be prevalent off the magnetic equator for externally driven toroidal modes), that are likely mixed together on this plot (band of orange/yellow color that extends across much of the plot with a trend of gradually decreasing frequency as L increases). Note that the plasmopause is typically expected at $L < 6$ (O'Brien & Moldwin, 2003).

Figure 1C shows the same data as in the second panel, but mean wave power in the wider Pc5, Pc4, and Pc3 frequency bands is shown to illustrate how averaging or integrating across the frequency band removes information about the normal mode spatial structure; this point will be discussed further in section 4. Finally, Figure 1D shows the result of a least squares fit of wave power to the Kp index at each frequency and spatial location (the result for a Kp value of 20 is shown, using the representation of Kp without decimal points from Matzka et al. (2021)), similar to the approach taken by Takahashi

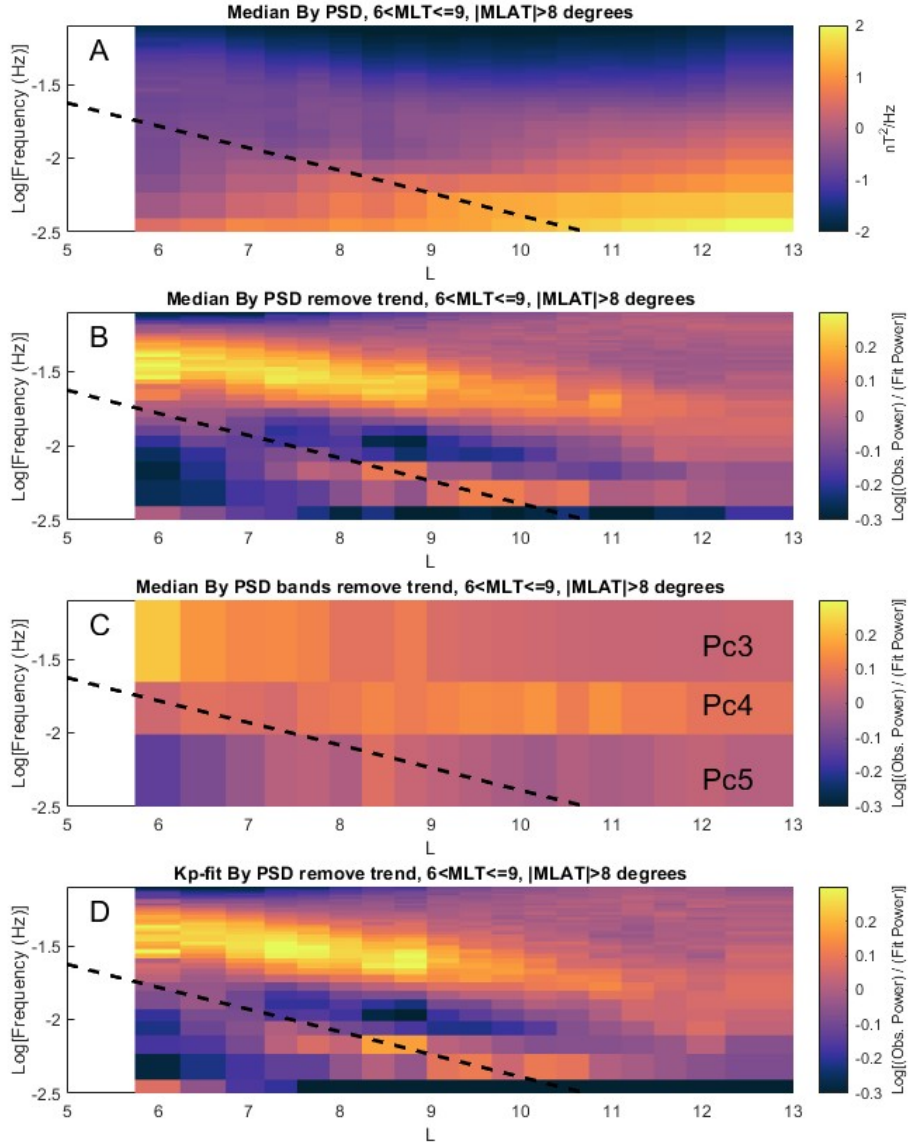


Figure 1. Example statistical results for the y component of the magnetic field in the $6 < MLT \leq 9$ sector and for magnetic latitudes greater than 8 degrees. A) median wave power in color as a function of frequency on the y-axis and radial distance on the x-axis. B) The same data as A, but in this case background trends are removed from each power spectrum prior to taking the median. C) The same data as A, but background trends are removed and mean values for the Pc5, Pc4, and Pc3 band are taken prior to taking the median. D) The same data as A, but in this case the result of robust fit of wave power to Kp at Kp=20 is shown rather than the median value. In each panel, a dashed black line indicates the predicted standing Alfvén wave frequency (fundamental mode).

and Anderson (1992) and the approach used by many radiation belt studies to obtain radial diffusion coefficients by first identifying relationships between ULF wave power and Kp, frequency, and L (e.g., Brautigam et al., 2005; Fei et al., 2006). As in panels B and C the wave power in panel D is normalized to a background trend, following the procedure of Takahashi and Anderson (1992); unlike in panels B and C and the rest of this study, the background power trend is obtained for the statistical results of wave power versus frequency rather than for individual DFT windows (see Takahashi and Anderson (1992) section 3.3 for further details). Though there are some small differences in wave power values, the results of the fit to Kp appear very similar to the median values (compare panels B and D of Figure 1). A Kp value of 20 is larger than the median value in our database but it is representative, and the results shown in panel D do not change significantly if values of 10, 13, or 17 are used instead of 20. Note that the median Kp obtained for the entire period from 1 Feb 2008 to 1 Dec 2020 is 13, while the median value in our database is slightly lower at 10 due to the removal of larger Kp events which often coincide with conditions when the THEMIS satellite is outside the magnetopause near apogee (we require THEMIS be inside the magnetosphere for a DFT window to be recorded since we are studying magnetospheric ULF waves).

In the remainder of this study, for simplicity we will only analyze wave power measurements using median values obtained after the subtraction of power law trends from individual spectra (i.e., like Figure 1B). This will allow us to focus on normal mode spatial structure and frequency rather than absolute amplitudes that may be dominated by transient magnetic disturbances, drift-mirror modes, and other magnetic disturbances with broadband frequency spectra. We note that our general conclusions hold when using a variety of methods (e.g., Figure 1D), and that many of the MHD normal mode features we describe are visible in median power spectra with no trend removal, though they are faint (e.g., the higher harmonic standing Alfvén waves in Figure 1A described above).

2.2 Numerical Simulations

We employ the numerical model of Wright and Elsden (2020), which solves the linear magnetohydrodynamic (MHD) equations for a cold plasma in a background dipole magnetic field. Full details of the model, including detailed descriptions of testing and the various choices made in the code development are given by Wright and Elsden (2020), with only the key properties summarised here. The model uses orthogonal, field-aligned coordinates (α, β, γ) , permitting high resolution both along and across the magnetic field. For comparison with the observations the coordinates correspond to the following directions: \mathbf{e}_γ is the field-aligned direction, referred to as \mathbf{e}_\parallel ; \mathbf{e}_β is the azimuthal direction, notated by \mathbf{e}_ϕ ; \mathbf{e}_α gives the outward normal direction on a given field line, but will be compared to the \mathbf{e}_r direction from the observations. The simulation coordinates \mathbf{e}_r , \mathbf{e}_ϕ and \mathbf{e}_\parallel are analogous to the data coordinates x , y and z .

The simulation domain is designed to study the dayside magnetosphere. The outer sunward boundary of the simulation is given by the location of the magnetopause in the equatorial plane using the Shue et al. (1997) model, from where the model is driven. The inner earthward boundary is set at $L = 5$, with a perfectly reflecting (node of radial velocity) boundary condition modeling a sharp change in the density at the plasmopause. The propagation of waves into the magnetotail is modeled with a dissipative region beyond $X = -6_{RE}$ (for X along the Earth-Sun line), such that waves which propagate into the tail do not return to the dayside solution region of interest. Only the northern hemisphere is solved for, with a symmetry condition applied at the equator for numerical efficiency, given that the model is driven symmetrically about the equator. The ionospheric boundary is further treated as reflecting. Dissipation is provided in the domain through the inclusion of resistivity to prevent small scales which develop through Alfvén wave phase mixing dropping below the grid resolution. The magnetopause boundary in all of the simulations presented here is driven in the same way, with continuous broad-

band perturbations ($\sim 0-50$ mHz) to the field-aligned magnetic field component B_{\parallel} . By driving in the same way in each simulation, we are able to compare the effect of the equilibrium (magnetopause location and density) on the wave solutions.

We have performed 11 simulations to be discussed in this manuscript, with the different setup criteria summarised in Table 1. Using three different subsolar magnetopause locations ($L_{mp} = 10, 11, 12$), and three Alfvén speed radial profiles with different gradients (shallow to steep, see SI Figure S3), yields nine simulations. Two further runs consider the effect of localised peaks in $V_A(L)$ at different L . Figure 2 gives an example output from the simulations, displaying the wave power at different frequencies of the azimuthal magnetic field B_{ϕ} as a function of L-shell, along the meridian MLT=8 and off the equator (see SI Figure S7). The quantity shown in this figure and subsequent simulation figures is the logarithm (base 10) of the magnitude of the DFT coefficient which has the units of nT; it is proportional to wave power. Note that the units of data figures (base 10 logarithm of the power ratio) and simulation figures (base 10 logarithm of the DFT magnitude in units of nT) differ, and they should not be compared quantitatively.

The rationale for our choice for the range $V_A(L)$ was motivated by past studies of $V_A(L)$ including Archer et al. (2015) (e.g., statistical results in Figure 1g in that study) and Archer et al. (2017) (e.g., examples in Figure 2 in that study), as well as visual inspection of $V_A(L)$ from events examined in our database. The values for $V_A(L)$ used in the simulations aren't representative of any single event, but rather they are meant to qualitatively explore trends in wave trapping, reflection, etc. due changing gradients and presence/absence of $V_A(L)$ peaks that are reasonable based on observations. The L_{mp} values used in the simulations are also meant to be representative of past studies of L_{mp} location and the range of L_{mp} in our database predicted by the Shue et al. (1997) model (the most likely L_{mp} in our database predicted by Shue et al. (1997) is 10.9 Earth radii); here, again, the range of values chosen is meant to qualitatively explore trends in normal mode structure while also being representative of typical observed L_{mp} values. For both $V_A(L)$ and L_{mp} , we do not attempt to simulate extreme cases (e.g., 99% of L_{mp} values lie between 6.7 and 13.2 Earth radii) though that is an important topic for future work. When more accurate information becomes available for $V_A(L)$ profiles (e.g., most work, including the present study, uses electron density observations with an assumed ion composition to obtain mass density thus $V_A(L)$) and better constraints on particular values for radial gradients, peak locations, etc., these should also be incorporated in future simulations for more direct, quantitative comparisons with observations. For example, while we have drawn from examples from case studies (e.g., Archer et al. (2017) Figure 2) and median statistical profiles (e.g., Archer et al. (2015) Figure 1g and 1h) to estimate the size and width of $V_A(L)$ peaks, it is likely that the properties of $V_A(L)$ peaks vary significantly from event to event depending on event-specific ion composition, plasmaspheric plume structure, etc.

Figure 2A is for a single simulation, with $L_{mp} = 11$ and weak V_A radial gradient. Dashed lines indicate the expected first, second, and third harmonic standing Alfvén wave frequencies calculated using simulation parameters (wave speeds); these lines compare very well with wave power enhancements, consistent with the presence of multiple standing Alfvén wave harmonics in this simulation. 2B is an average of nine simulations for the different permutations of the three magnetopause locations and three $V_A(L)$ gradients; in this case, the dashed lines are averages of the calculated standing Alfvén wave frequencies for the three different Alfvén speed profiles reflected in the simulation ensemble. Clear frequency bands are present showing the different harmonics in both panels, but in panel B these bands are somewhat blurred due to the averaging across the different simulations. Supporting Information Figures S4-6 show results for each of the 9 simulations used in the average. Note that we are using average, or arithmetic mean, values for ensemble analysis of simulation measurements as there are too few simulation

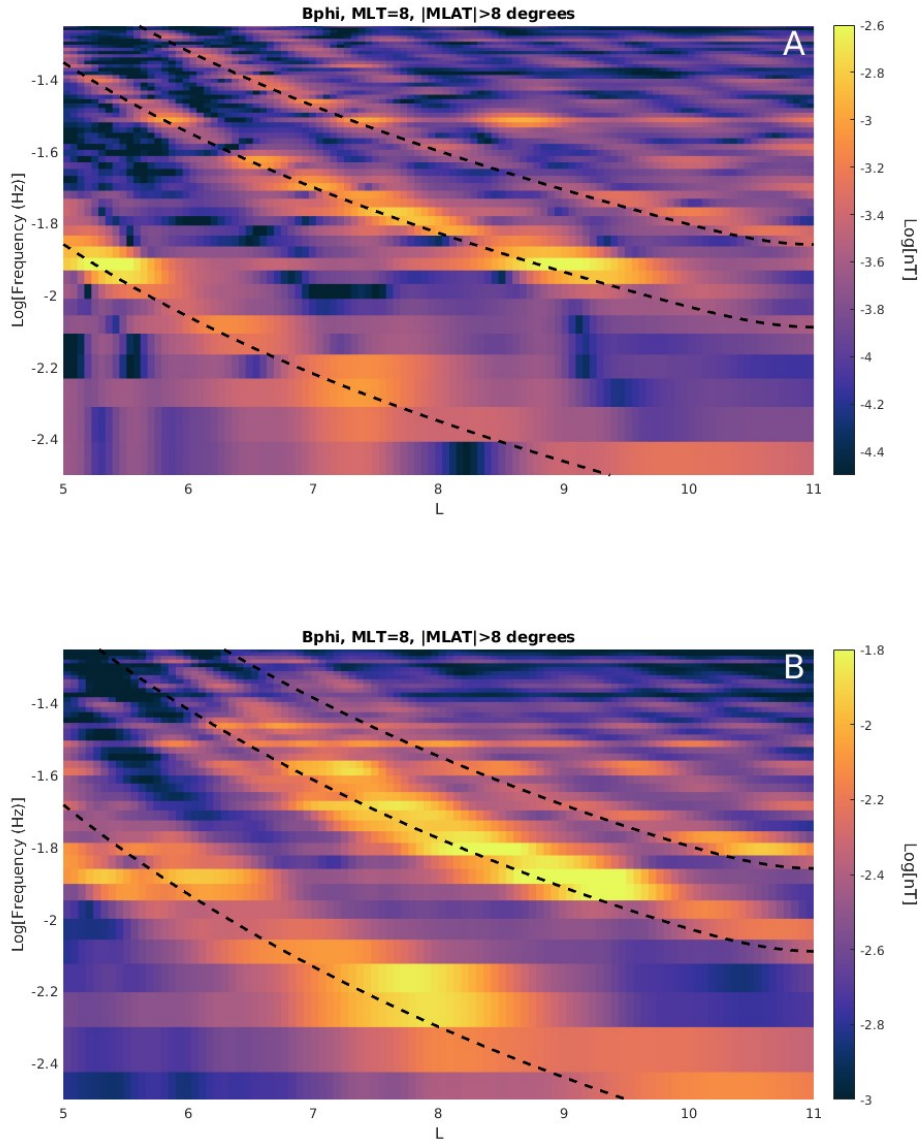


Figure 2. A) Simulated meridional wave power for the ϕ component of the magnetic field in the MLT=8 meridian averaged for magnetic latitudes greater than 8 degrees; the results shown correspond to a single simulation, number 4 in Table 1, with dashed lines indicating the first, second, and third harmonic standing Alfvén wave frequencies. B) The same format as panel A but instead showing the average of an ensemble of 9 simulations (Numbers 1-9 in Table 1), including the simulation in panel A. In this case, the dashed lines are averages of the standing Alfvén wave frequencies calculated for the three different Alfvén speed profiles reflected in the simulation ensemble. The individual results for each of the 9 simulations are shown in SI Figures S4, S5, and S6.

Table 1. Summary of the Numerical Simulations Used in This Study

Description	Va Radial Gradient	Local Va peak	Subsolar Magnetopause
1 - Shallow Va, Small Lmp	Shallow	None	L=10
2 - Moderate Va, Small Lmp	Moderate	None	L=10
3 - Steep Va, Small Lmp	Steep	None	L=10
4 - Shallow Va, Medium Lmp	Shallow	None	L=11
5 - Moderate Va, Medium Lmp	Moderate	None	L=11
6 - Steep Va, Medium Lmp	Steep	None	L=11
7 - Shallow Va, Large Lmp	Shallow	None	L=12
8 - Moderate Va, Large Lmp	Moderate	None	L=12
9 - Steep Va, Large Lmp	Steep	None	L=12
10 - Peak Va 6, Medium Lmp	N/A	L=6	L=11
11 - Peak Va 9, Medium Lmp	N/A	L=9	L=11

434 runs to obtain meaningful median values. Throughout the rest of the study, we will use
 435 median values to represent the distribution of observed wave power values in different
 436 conditions and spatial regions (previous section), while mean values will serve the same
 437 purpose for ensemble simulation runs. The use of these two different quantities will not
 438 affect our conclusions as we only rely on qualitative comparisons between simulations
 439 and observations.

440 3 Results

441 In this section, we examine how different magnetospheric equilibria affect normal
 442 mode properties using both observations and numerical simulations, focusing on two pa-
 443 rameters that are known to control ULF wave properties (section 1): magnetopause lo-
 444 cation and radial Alfvén speed profile. We will also analyze results for a broader set of
 445 conditions as a point of reference.

446 3.1 Results for a Broad Range of Conditions

447 Figure 3 is for average values from an ensemble of 9 simulations with different mag-
 448 netopause locations and radial Alfvén speed gradients (simulations 1-9 in Table 1, see
 449 SI Figure S3 for radial Alfvén speed profiles); the results for individual simulations are
 450 shown in SI Figures S4-6. Figure 3A-C is for the MLT=8 meridian and regions near the
 451 magnetic equator (magnetic latitude less than 5 degrees); average wave power is shown
 452 in color as a function of frequency (y-axis) and radial distance (x-axis) for the radial (panel
 453 A), azimuthal (panel B), and parallel (panel C) magnetic field components. In panel B,
 454 discrete frequency peaks are seen with frequency that decreases with increasing radial
 455 distance as expected for standing Alfvén waves. In panel C, discrete frequency peaks ap-
 456 pear that are consistent with expectations for cavity/waveguide modes, including (1) the
 457 local minima and maxima in wave power as a function of radial distance that differ from
 458 expectations for surface waves and disturbances originating from the magnetopause which
 459 would have monotonically decaying wave power with distance from the magnetopause
 460 and (2) the constant frequency with radial distance that differs from expectations for stand-
 461 ing Alfvén waves. Though the features in Figure 3A-C are consistent with normal modes,
 462 they are blurred together consistent with the ensemble average. The lowest frequency
 463 peak in Figure 3C has a radial structure consistent with a quarter wavelength cavity/waveguide
 464 mode, in particular a power peak near the inner boundary of the simulation. This is due

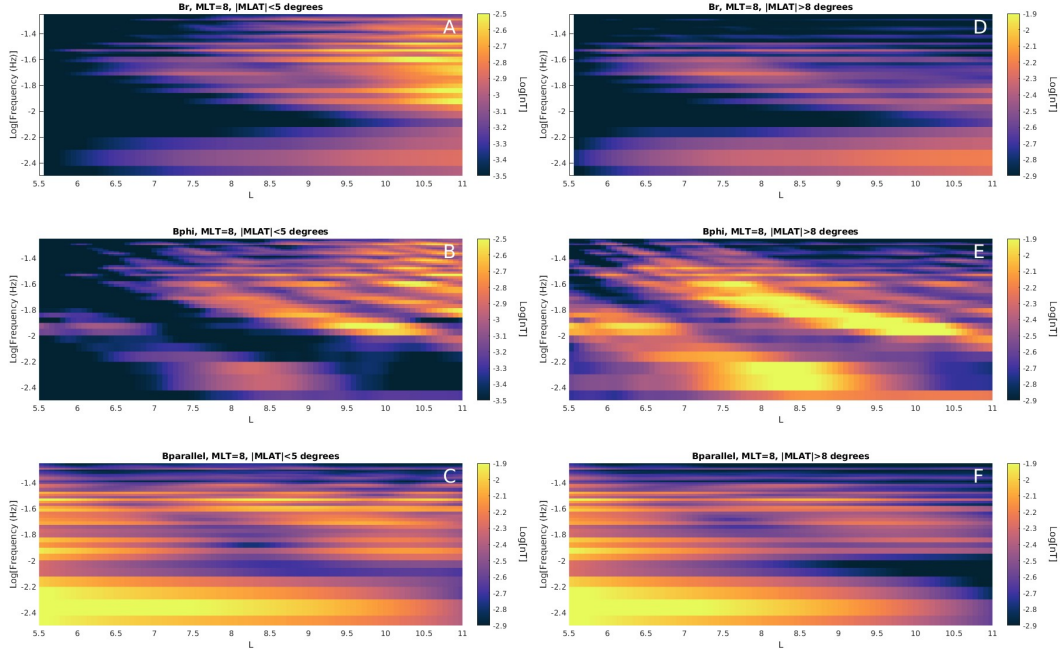


Figure 3. Ensemble average simulation results (simulations 1-9 in Table 1). A) Wave power along the MLT=8 meridian on the magnetic equator ($|MLAT| < 5$ degrees) for the magnetic variations in the radial magnetic field. B) The same as A, but for azimuthal magnetic field. C) The same as A, but for the component parallel to the background magnetic field. D, E, F) The same as A, B, C but for locations off the magnetic equator ($|MLAT| > 8$ degrees).

465 to the use of a perfectly reflecting boundary condition at $L=5$ (node in radial velocity,
 466 anti-node or peak in parallel magnetic field).

467 Figure 3D-F is the same as 3A-C but for regions off the magnetic equator (mag-
 468 netic latitude greater than 8 degrees) and using a different colorbar to account for larger
 469 wave power in some panels. In particular, discrete frequency wave power in the azimuthal
 470 magnetic field seen in panel E is significantly larger than in panel B as expected for odd
 471 harmonics of toroidal mode standing Alfvén waves. As before, however, the features are
 472 blurred together. These results can be compared against SI Figures S4-6 which show much
 473 narrower and distinct discrete frequency peaks in the individual simulations that make
 474 up the average shown in Figure 3.

475 The results in Figure 3 are qualitatively consistent with what might be expected
 476 when statistically analyzing wave measurements that include a range of different driv-
 477 ing conditions. However, it is not obvious whether similar trends would be seen in ob-
 478 servations at higher L values near the magnetopause given expectations in that region
 479 for significant variability in the radial Alfvén speed profile (Archer et al., 2015), mag-
 480 netopause geometry (Shue et al., 1997), and the presence of drift-mirror modes and other
 481 magnetic disturbances unrelated to normal modes (Zhu & Kivelson, 1991). Figure 4 shows
 482 that, despite the presence of this variability, median wave power spectra can indeed re-
 483 veal normal mode structure and are at least qualitatively consistent with the simulations.
 484 In particular, Figure 4A-C is in the same format as Figure 3A-C, showing median wave
 485 power as a function of radial distance (x-axis) and frequency (y-axis) for regions near
 486 the magnetic equator (magnetic latitude less than 5 degrees). From top to bottom, re-
 487 sults are shown for the radial (panel A), azimuthal (panel B), and parallel (panel C) mag-

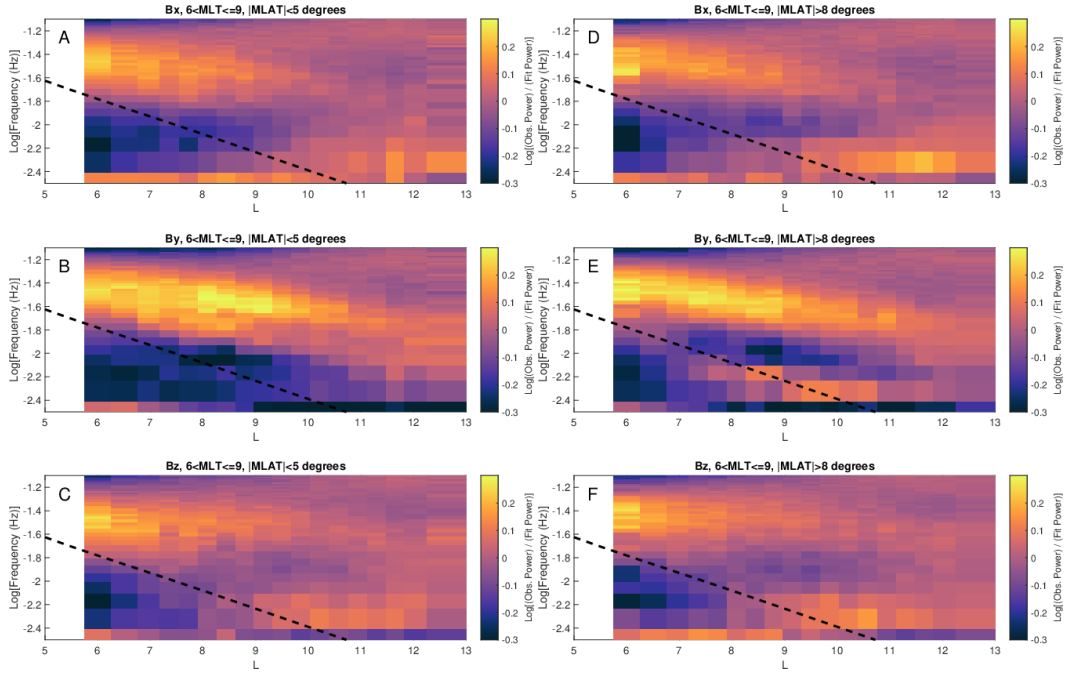


Figure 4. A) Median wave power in the x component (radial in MFA coordinates) in the $6 < MLT \leq 9$ sector and for magnetic latitudes less than 5 degrees. A dashed black line indicates the predicted standing Alfvén wave frequency (fundamental mode). B) The same as A, but for the y component (azimuthal). C) The same as A, but the the z component (parallel to background magnetic field). D, E, F) The same as A, B, C but for locations off the magnetic equator ($|MLAT| > 8$ degrees).

488 netic field, and a dashed line in all panels indicates the expected frequency for a funda-
 489 mental toroidal mode using the same approximation as in Figure 1. In Figure 4B, two
 490 broad peaks in wave power are observed above the predicted fundamental mode frequency
 491 (dashed line) that blur together at low radial distances. Both peaks have frequency de-
 492 creasing with increasing radial distance, consistent with standing Alfvén waves. These
 493 peaks have frequencies that are consistent with second and third harmonic toroidal waves.
 494 Little power is observed at frequencies expected for fundamental mode standing Alfvén
 495 waves (dashed line), consistent with the expected location of a node (local minima) in
 496 wave power near the magnetic equator (Sugiura & Wilson, 1964; Sarris et al., 2022). The
 497 blurring of these features that becomes more pronounced at smaller radial distances is
 498 due at least in part to the increase in the variation of eigenfrequencies closer to the Earth
 499 (e.g., Archer et al., 2015; Takahashi et al., 2015).

500 Figure 4C is for the parallel magnetic field component, with two broad, constant
 501 frequency peaks in wave power observed that include local minima and maxima as a func-
 502 tion of radial distance. As was the case with the simulations, these features are consis-
 503 tent with cavity/waveguide modes, with the blurred features suggesting that there is sig-
 504 nificant variability in the frequency of cavity/waveguide modes reflected in the median
 505 values. Concerning the higher frequency peak, the blurring and general preference for
 506 a subset of the Pc3-4 frequency band may also be due in part to the energy source(s)
 507 for these waves. For example, upstream waves (waves associated with the ion foreshock)
 508 have a finite bandwidth that usually extends across much of the Pc3-4 range; though mag-
 509 netospheric waves associated with upstream waves are generally expected to have max-
 510 imum amplitudes close to the outer boundary, magnetospheric cavity modes with peak
 511 compressional magnetic field perturbations deep inside the magnetosphere similar to what’s
 512 seen in Figure 4C can also be driven by upstream waves (Takahashi et al., 2010). One
 513 would generally expect to see a mixture of the driving energy spectrum and the normal
 514 modes in these plots. The compressions seen in Figure 4C may also be due in part to
 515 poloidal mode Alfvén waves which are known to be associated with magnetic compres-
 516 sions in realistic magnetic field geometries (e.g., Dai et al., 2015). The lower frequency
 517 peak in Figure 4C is also likely associated with a cavity/waveguide mode, though, as with
 518 the higher frequency peak, it may well include contributions from other wave modes such
 519 as magnetopause surface waves associated with the Kelvin-Helmholtz instability and mag-
 520 netopause surface eigenmodes which can have frequencies that extend into the Pc5 range
 521 (Plaschke & Glassmeier, 2011). In section 3.3, we will show conclusively that both of these
 522 features, while including some contributions from other wave modes, exhibit behavior
 523 that can only be related to normal modes.

524 Figure 4D-F is the same as the A-C but for locations off the magnetic equator (mag-
 525 netic latitude greater than 8 degrees). The most significant difference appears in panel
 526 E, where a discrete frequency peak in wave power is seen that matches the expected fre-
 527 quency dependence of the fundamental toroidal mode (wave power enhancement near
 528 dashed black line). As was the case for the simulations, the much larger wave power in
 529 the fundamental mode off the magnetic equator is expected for the odd mode structure
 530 with node in magnetic field perturbation at the magnetic equator. It is also consistent
 531 with trends seen in recent observational work examining band-integrated wave power (e.g.,
 532 Sarris et al., 2022). The fact that the peak in power along this dashed line is just inside
 533 the location with peak Pc5 power in Figure 4C that was associated with a cavity/waveguide
 534 mode (see above) further suggests that cavity/waveguide modes may be coupling to toroidal
 535 modes via field line resonance to produce these features. It’s also worth noting that in
 536 contrast to the two peaks in power above the predicted fundamental mode frequency that
 537 were seen in regions close to the magnetic equator (Figure 4B), only the highest frequency
 538 peak is seen in 5E; this is further evidence that the lower frequency peak seen in Fig-
 539 ure 4B was consistent with a second harmonic mode, as a lower amplitude is expected
 540 for this mode off the magnetic equator. Finally, the peaks in power in Figure 4F have
 541 some similarities to Figure 4C; these are likely caused by the same types of wave activ-

ity, though perhaps with different relative contributions from the Alfvén mode, cavity/waveguide mode, etc. Note that both Figure 4C and 4F do not have the peak in power at low frequencies near $L=5$ seen in the simulations (compare with Figure 3C and 3F); this is likely due to the use of a perfectly reflecting inner boundary at $L=5$ in the simulations, as discussed above.

Taken together, Figures 3 and 4 show that normal modes can be sustained in the magnetosphere in a wide range of conditions, but due to having properties that vary from event to event they are blurred together in statistical analysis when examining median values that include all conditions. The presence of more discrete frequency peaks and smaller spatial scale features in the ensemble average simulation output (Figure 3) reflects the fact that we have only run nine simulations where variability is only represented by three different radial Alfvén speed profiles and three different magnetopause locations. If we had incorporated, for example, 1000 simulations with wider range of conditions the features would invariably blur further and be more consistent with the observations in Figure 4. Nevertheless, Figure 4 shows that normal mode structure is evident even in median wave power spectra; this is somewhat remarkable when considering the variability expected in this region, for example, in the magnetopause location (Shue et al., 1997; Murphy et al., 2015; Sandhu, Rae, Staples, et al., 2021), radial Alfvén speed profile (Archer et al., 2015; Wharton et al., 2019; Sandhu, Rae, Staples, et al., 2021), and other parameters.

3.2 Different Radial Alfvén Speed Profiles

The numerical simulations in section 3.1 used radial Alfvén speed profiles that decreased monotonically with increasing radial distances throughout the simulation domain. In this section, we consider profiles with local peaks (x_{ib} location) at 6 Re and 9 Re (radial Alfvén speed profiles shown in SI Figure S7). Figure 5A-C is the same format as the 3A-C (MLT=8, magnetic latitude less than 5 degrees), but for a single simulation where the Alfvén speed profile has a peak near the inner boundary at $L=6$ Re; as was the case in Figure 3, discrete frequency peaks are seen in Figure 5B with decreasing frequency as radial distance increases, though the frequency varies more slowly near the Alfvén speed peak at $L=6$ (compare Figure 3B to Figure 5B). Dashed lines in Figure 5B are for the frequencies calculated for the first, second, and third standing Alfvén harmonics using the Alfvén speeds in the simulations; the close correspondence between these lines and the discrete frequency power enhancements provides further evidence for the presence of standing Alfvén waves. Figure 5D-F is for the case where the local Alfvén speed peak is at $L=9$ Re. This significantly alters the normal mode structure in several ways: (1) the frequency of all normal modes changes, (2) the standing Alfvén wave frequency first increases, then flattens, then decreases with increasing radial distance when the peak is at larger L values (compare panels B and E in Figure 5), (3) the maxima in wave power for radial (panels A and D) and compressional (panels C and F) components changes location, with significant wave power trapped inside the location of the Alfvén speed peak when located at $L=9$ (Figure 5F).

Figure 6 is for median wave power for situations when x_{ib} (peak Alfvén speed in each data segment, see section 2) is at $5 < x_{ib} < 7$ Re (panels A,B,C) or $8 < x_{ib} < 10$ Re (panels D,E,F). For comparison, Supporting Information Figure S8 obtains x_{ib} using the empirical model of Archer et al. (2017), with similar results. The same MLT region is shown as in Figure 4A-C ($6 < MLT \leq 9$), but, unlike in Figure 4, all magnetic latitudes are included to obtain enough data for meaningful statistical results. There are 22350 samples (DFT windows) in this local time sector, with 8405 (37.6%) and 5120 (22.9%) samples in the $5 < x_{ib} < 7$ Re and $8 < x_{ib} < 10$ Re bins, respectively; thus, these locations for x_{ib} occur frequently in this sector. This is consistent with results from past work, including Archer et al. (2017) and the empirical modeling of Moore et al. (1987)

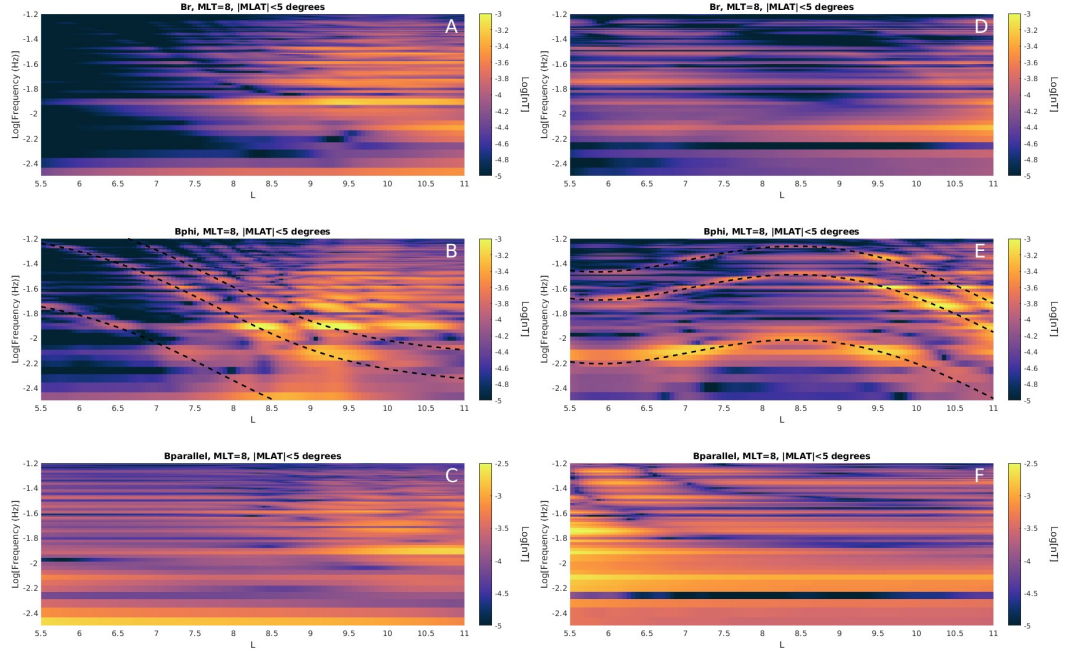


Figure 5. A) Wave power results in the radial component are shown for the $MLT = 8$ sector and magnetic latitudes less than 5 degrees for a simulation where a local peak in the radial Alfvén speed profile is at a radial distance of $6 R_E$. B) The same as A, but for the azimuthal component. Dashed lines are for calculated standing Alfvén wave frequencies for the first, second, and third harmonics. C) The same as A, but for the component parallel to the background magnetic field. D,E,F) The same as for A,B,C, but results are shown for a simulation where the local peak in the radial Alfvén speed profile is at $9 R_E$.

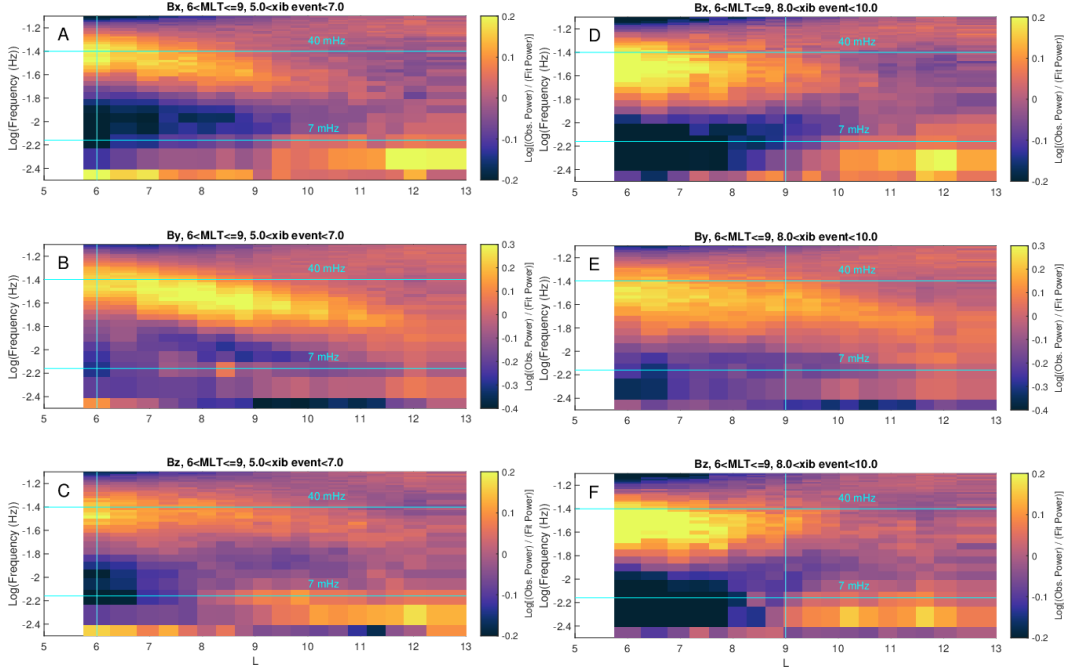


Figure 6. A) Median wave power in the x component (radial in MFA coordinates) in the $6 < MLT \leq 9$ sector and conditions where the local maximum in the radial Alfvén speed profile, x_{ib} , is in the range $5.0 < x_{ib} < 7.0$. A vertical blue line marks the center of the range of x_{ib} values, $6.0 R_E$, while horizontal dashed lines are shown at values of 7 and 40 mHz. B) The same as A, but for the y component (azimuthal). C) The same as A, but the the z component (parallel to background magnetic field). D,E,F) The same as A,B,C, but for $8.0 < x_{ib} < 10.0$. The vertical blue line is now at $9 R_E$, the center of the x_{ib} range.

593 which nominally puts the dawn sector peak at $\sim 7R_E$ (Figure 2A in that study), though
 594 as noted in section 2 there is considerable variability in peak location from event to event.

595 As in Figure 4, Figure 6A-C exhibits evidence of normal modes: (1) discrete fre-
 596 quency peaks with decreasing frequency as radial distance increases in the middle panel
 597 consistent with standing Alfvén waves and (2) constant frequency peaks with nodes/anti-
 598 nodes in the bottom panel consistent with cavity/waveguide modes. Similar evidence of
 599 normal modes is also found in Figure 6D-F ($8 < x_{ib} < 10$), but there are significant
 600 differences now that x_{ib} is at higher radial distances: (1) significant wave energy in the
 601 radial (panel D) and parallel (panel F) magnetic field found inside the peak location at
 602 frequencies in the Pc4 and lower Pc3 frequency ranges with comparatively less power in
 603 the outer magnetosphere, (2) less Pc5 wave energy in the parallel magnetic field at low
 604 radial distances when x_{ib} is at large radial distances (i.e., decreased ability for fast mode
 605 waves at lower frequencies to penetrate to the inner magnetosphere, compare panel C
 606 to panel F), and (3) the discrete frequency peaks that were seen in the azimuthal mag-
 607 netic field (Figure 6B) are much broader and only exhibit a clear trend of decreasing fre-
 608 quency with increasing radial distance at radial distances larger than the radial Alfvén
 609 speed peak ($L > \sim 10 R_E$).

610 The simulations in Figure 5 and the data in Figure 6 both show consistent changes
 611 in normal mode properties as the local peak in the radial Alfvén speed profile changes
 612 location: (1) flat or non-monotonically decreasing standing Alfvén wave frequencies when

613 there's a peak at larger radial distance, (2) increased compressional wave trapping in the
 614 inner magnetosphere (inside the Alfvén speed peak) when the peak is at larger radial
 615 distances. There are some differences between the data and simulations, likely because
 616 (1) we are comparing statistical results against individual simulations rather than an en-
 617 semble of simulations and (2) the simulated Alfvén speed profiles and inner boundary
 618 location are not fully representative of nominal conditions in the magnetosphere. Nev-
 619 ertheless, taken together, these results show that theoretical predictions for the alteration
 620 of MHD normal mode structure in the presence of different radial Alfvén speed peak lo-
 621 cations are consistent with the data. Conditions with $x_{ib} > 6.0$ Earth radii occur fre-
 622 quently in the outer magnetosphere (Archer et al., 2015, 2017) and should be considered
 623 more carefully in space weather models that rely on ULF wave fields (see section 4).

624 3.3 Different Subsolar Magnetopause Locations

625 In this section, we consider how subsolar magnetopause location affects MHD nor-
 626 mal mode structure. As in previous simulation Figures, Figure 7 shows wave power in
 627 the $MLT=8$ meridian as a function of radial distance on the x-axis and frequency on the
 628 y-axis. Here, all panels are for magnetic latitudes below 5 degrees and for wave power
 629 in the parallel component of the magnetic field. Figure 7A is identical to Figure 3C and
 630 is for the ensemble average of simulations 1-9 in Table 1, including conditions where the
 631 subsolar magnetopause is at 10, 11, and 12 Re; it is shown for reference to compare against
 632 simulations for specific magnetopause locations. Figure 7B is for an average of simula-
 633 tions 1-3 in Table 1, all of which have a subsolar magnetopause at 10 Re. Though ap-
 634 pearing qualitatively similar to panel A, there are a few differences: (1) no simulation
 635 output (white space) in outermost L values due to the flank magnetopause moving in-
 636 ward, (2) sharper discrete frequency peaks in wave power with somewhat different peak
 637 power locations when compared to the top panel, (3) overall more wave power at low L
 638 values. Figure 7C is for an average of simulations 4-6 in Table 1, all of which have sub-
 639 solar magnetopause locations at 11 Re. As with panel B, the discrete frequency peaks
 640 in wave power are overall sharper than in panel A. Additionally, the peak wave power
 641 locations have shifted somewhat when compared to panels A and B. Similar differences
 642 are again seen in Figure 7D which is for an average of simulations 7-9 in Table 1, all of
 643 which have subsolar magnetopause locations at 12 Re. Comparing panels B, C, and D,
 644 one other trend is obvious as the subsolar magnetopause is shifted outward: a tendency
 645 for discrete frequency peaks to shift to lower frequencies as the magnetopause moves out-
 646 ward, seen most obviously when comparing the lowest frequency peaks in each panel.
 647 Taken together, the results in Figure 7 show that normal modes in the compressional mag-
 648 netic field (cavity/waveguide/virtual resonance) exist for all magnetopause locations, but
 649 their properties change as the magnetopause location changes: generally decreasing fre-
 650 quency with increasing magnetopause location and changing location of nodes/anti-nodes.
 651 The lower frequency with larger magnetopause location is expected due to (1) the larger
 652 magnetopause cavity and (2) the smaller magnetic field, thus Alfvén speed, expected when
 653 the magnetopause located is further out and the magnetosphere is less compressed (Archer
 654 et al., 2017).

655 Figure 8 tests whether the trends in Figure 7 can be seen in data. Figure 8A shows
 656 median wave power in the parallel component of the magnetic field as a function of ra-
 657 dial distance on the x-axis and frequency on the y-axis in the $6 < MLT \leq 9$ sector;
 658 horizontal and vertical blue lines are for reference as discussed below. The results are
 659 similar to Figure 4C, except that all magnetic latitudes are included in order to be con-
 660 sistent with other panels (as in Figure 6, this is needed to ensure sufficient data cover-
 661 age). As discussed in section 3.1, evidence of cavity/waveguide modes is seen in the form
 662 of discrete frequency peaks in wave power with nodal structures that do not change their
 663 frequency as radial distance changes. Figure 8B is for median wave power when the sub-
 664 solar magnetopause obtained from the Shue et al. (1997) model is between 8.5 and 10
 665 Re. Discrete frequency peaks are again seen but with different frequencies and different

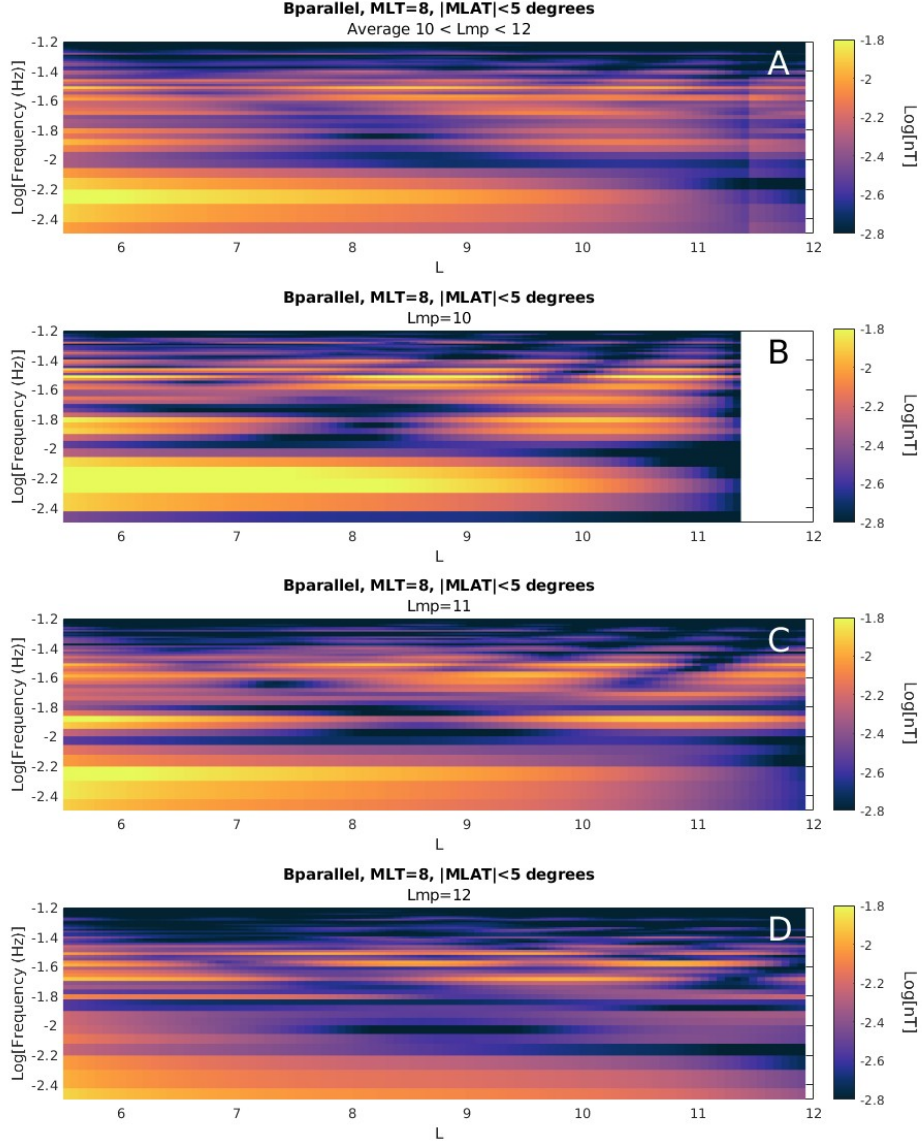


Figure 7. A) Average wave power in the parallel component of the magnetic field across simulations 1-9 in Table 1; the results are shown as a function of radial distance in the $MLT = 8$ sector and for magnetic latitudes below 5 degrees. B) The same as A, but the average wave power is only calculated using simulations with subsolar magnetopause at $L = 10$ (1-3 in Table 1). C) The same as A, but the average wave power is only calculated using simulations with subsolar magnetopause at $L = 11$ (4-6 in Table 1). D) The same as A, but the average wave power is only calculated using simulations with subsolar magnetopause at $L = 12$ (7-9 in Table 1).

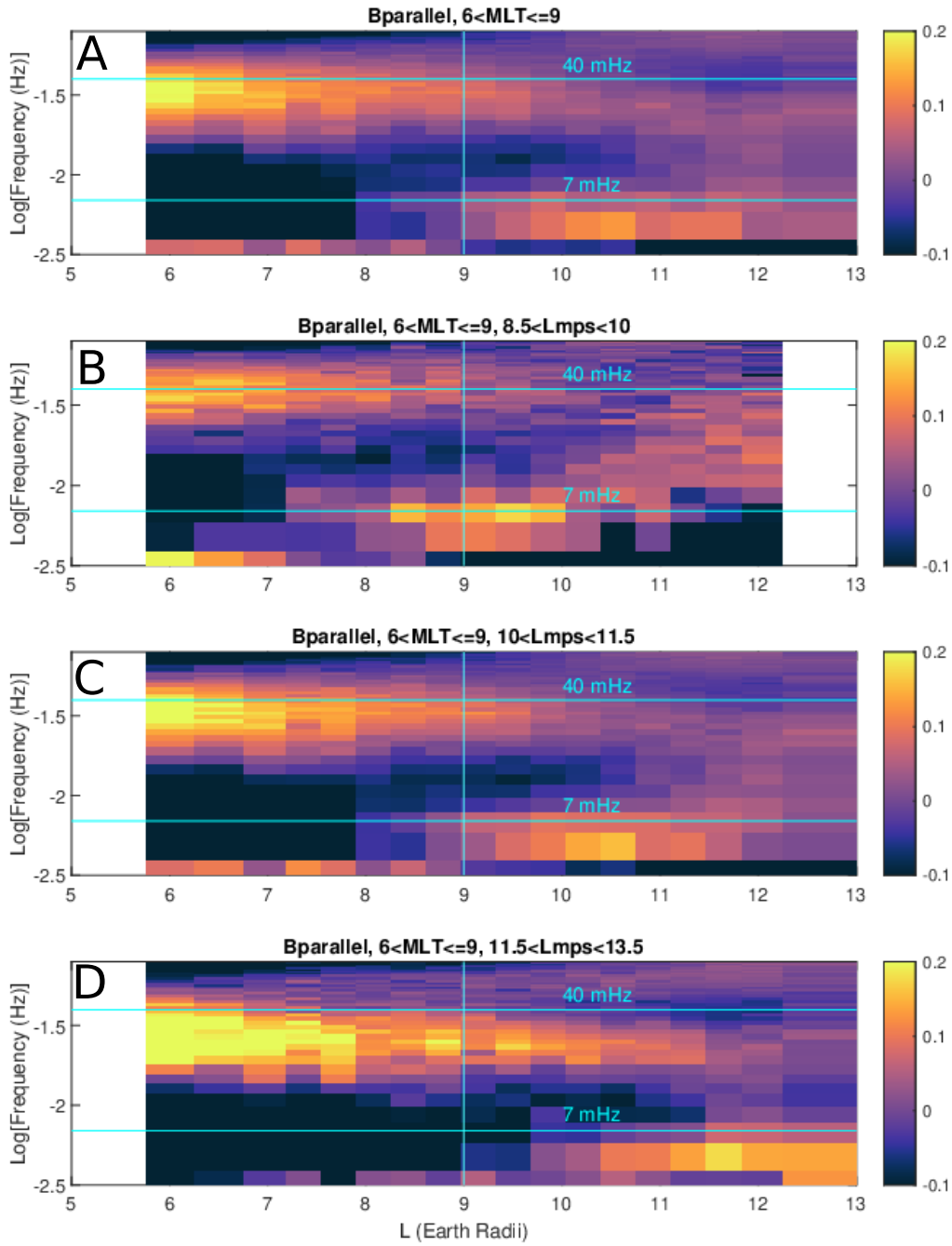


Figure 8. A) Median wave power in the parallel magnetic field component as a function of radial distance in $6 < MLT \leq 9$ sector. A vertical blue line marks $9.0 R_E$, while horizontal dashed lines are shown at values of 7 and 40 mHz. B) The same as A, but only including measurements during conditions when the subsolar magnetopause as determined by the Shue et al. (1997) model is in the range $8.5 < L_{mp} < 10.0$. C) The same as B, but for $10 < L_{mp} < 11.5$. D) The same as B, but for $11.5 < L_{mp} < 13.5$.

666 locations of nodes and anti-nodes. The horizontal blue lines mark the approximate cen-
 667 ter frequencies of two harmonics, and the vertical line marks the approximate radial dis-
 668 tance of the anti-node (local maxima) associated with the lower frequency harmonic; these
 669 lines are also shown in other panels to highlight changes in frequency and spatial struc-
 670 ture as the magnetopause location changes. Figure 8C is for median wave power when
 671 the subsolar magnetopause is between 10 and 11.5 Re; compared with panel B, the fre-
 672 quencies have shifted lower and the anti-node has moved outward. These trends continue
 673 in panel D, which is for median wave power when the magnetopause is between 11.5 and
 674 13.5 Re; the frequencies of the harmonics have shifted lower, with anti-nodes at still higher
 675 radial distances. Figure 8 provides firm evidence of cavity/waveguide modes in the outer
 676 magnetosphere; transient disturbances and other MHD wave modes could not explain
 677 these discrete frequency peaks with nodal structure and properties (location of nodes,
 678 frequencies) that change according to magnetopause location. Note that the bins chosen
 679 for subsolar magnetopause location are consistent with the typical range of values
 680 seen in the dataset; there are 22350 DFT samples in the $6 < MLT \leq 9$ sector, with
 681 2562 (11.5%), 14335 (64.1%), and 5073 (22.7%) samples occurring when $8.5 < L_{mp} <$
 682 10.0 , $10. < L_{mp} < 11.5$, and $11.5 < L_{mp} < 13.5$, respectively. However, the exact
 683 choice of bin range for L_{mp} is somewhat arbitrary (e.g., 13.0 could have been used in-
 684 stead of 13.5 without changing the results) with the main criteria being (1) that there
 685 were sufficient samples in each bin to explore the L variation of normal mode structure
 686 and (2) that the bins were sufficiently different that changing normal mode structure due
 687 changing L_{mp} could be observed. Future work exploring quantitative comparisons be-
 688 tween observations and simulations should adjust these bin ranges and the correspond-
 689 ing simulation outer boundary location for better agreement.

690 Taken together, the results in Figures 7 and 8 show how the location of the mag-
 691 netopause affects the properties of MHD normal modes. In contrast to results found for
 692 band-integrated ULF wave power in past studies (section 1), normal mode amplitudes
 693 do not decay monotonically with distance from the magnetopause, and a smaller sub-
 694 solar magnetopause does not always mean normal mode wave power will be larger at smaller
 695 radial distances. When considering whether wave amplitude associated with cavity/waveguide
 696 modes will be larger at a given frequency and radial distance, one needs to consider the
 697 interplay between the amount of energy being delivered to the normal mode and the fre-
 698 quency and spatial dependence of the normal mode structure. For example, a key dif-
 699 ference between the simulation results in Figure 7 and the observed results in Figure 8
 700 is that power enhancements tend to occur near 40 mHz in the observations, whereas in
 701 the simulations there is no clear preference near 40 mHz. It is possible that the observed
 702 power enhancements near 40 mHz are related to upstream wave activity in the ion fore-
 703 shock (Takahashi et al., 1984); this energy source is not present in the simulations which
 704 use an energy source with a broadband frequency spectrum. Thus, though observations
 705 and simulations both indicate normal mode activity with frequency and spatially depen-
 706 dence on magnetopause location, the observations are also affected by a frequency de-
 707 pendent energy source.

708 4 Discussion

709 In this study, we statistically analyzed wave power spectra from magnetic field mea-
 710 surements made by the THEMIS satellites and compared with individual and ensem-
 711 ble average numerical simulation results. We identified frequency and spatial-dependent
 712 normal mode structure in the region $5 < L < 13$ consistent with theoretical expecta-
 713 tions for MHD normal modes. It is somewhat remarkable that these features, while blurred
 714 somewhat compared to numerical simulations, are apparent in observed median wave power
 715 spectra when considering the variability in normal mode properties expected in magne-
 716 topause location, radial Alfvén speed profile, and driving condition, all of which control
 717 their frequency and spatial structure. We further showed how the properties of stand-

ing Alfvén waves and cavity/waveguide modes changed when restricting to specific magnetopause locations and specific locations of radial Alfvén speed profile peaks, finding significant changes in locations of nodes/antinodes, frequencies, and other properties.

The results presented in section 3.2 show that the properties of the radial Alfvén speed profile, represented by the x_{ib} parameter corresponding to the radial distance of the peak Alfvén speed at $L > 5$, significantly impact both standing Alfvén wave properties and cavity/waveguide mode properties. Trends observed in numerical simulations (Figure 5) as the peak moves outward such as the flattening/blurring of the radial dependence of standing Alfvén wave frequency and the trapping of compressional wave energy are also qualitatively seen in the data (Figure 6). Past theoretical and numerical simulation work showed that the location of x_{ib} , along with wave frequency and spatial scale, affects the trapping of wave energy and ability to penetrate from the outer magnetosphere to the inner magnetosphere. All things equal, lower frequency waves become evanescent at larger radial distances than higher frequency waves. This is seen in Figure 6; as x_{ib} is moved outward (compare left to right panel), wave power in the radial (top panel) and parallel (bottom panel) components at frequencies below 7 mHz is reduced. This suggests that x_{ib} could be used to organize wave measurements more effectively than, for example, the electron density plasmopause.

The results presented in section 3.3 show that the magnetopause location - already known to affect a variety of ULF wave properties - affects not only the frequency (e.g., Murphy et al., 2015; D. Zhang et al., 2023) but also the spatial structure of cavity/waveguide modes in the outer magnetosphere. This was expected from theoretical predictions and numerical simulations (e.g., Figure 7), but direct observational evidence of this changing spatial structure was missing likely due to (1) the relatively small amplitudes of cavity/waveguide modes in the outer magnetosphere making them less obvious in case studies or statistical analysis that includes other ULF waves (M. D. Hartinger, Angelopoulos, et al., 2013), (2) the lack of a large dataset needed to achieve meaningful statistics at a wide range of radial distances and for subsets of magnetopause locations, and (3) the frequency resolution needed to resolve the changing frequency and node/antinode locations (Figure 8) which could not be seen with band-integrated power in, for example, the Pc5, Pc4, and Pc3 ranges (e.g., Figure 1).

These results have potentially important implications for space weather models seeking to capture the effects of MHD normal modes on inner magnetosphere particle populations. Magnetospheric Pc4-5 waves (2-22 mHz) have the appropriate frequencies and phase speeds for drift and drift-bounce interactions with radiation belt electrons (e.g., Elkington et al., 2003; Zong et al., 2017). When a continuum of wave frequencies/modes are present, this radial transport can be described via a diffusion approximation, with several models employing numerous methods for parameterizing the wave fields via radial diffusion coefficients (Ozeke et al., 2014; Lejosne & Kollmann, 2020; Drozdov et al., 2021). For example, Fei et al. (2006) show that the diffusion coefficients depend in part on wave power at different frequencies and azimuthal wave numbers; radial diffusion coefficient formulations such as in Fei et al. (2006) are in effect assuming MHD waves with phase speeds comparable to relativistic electron drift speeds. However, in practice the techniques used to obtain wave power are not designed to separate these waves - including normal modes which are usually invoked as the mechanism causing drift resonance (e.g., Elkington et al., 1999, 2003; Zong et al., 2017) - from other magnetic disturbances that are not in resonance. This is undesirable for two related reasons:

1. Other ULF wave modes affect radiation belt dynamics in different ways from normal modes thus should ideally not be included in radial diffusion coefficient formulations based on wave power observations. For example, drift-mirror modes do not satisfy drift resonance as they drift at speeds far lower than typical relativistic electron drift speeds. Instead, these compressional waves transport populations

770 of hot, anisotropic ions and electrons, naturally unstable to electromagnetic ion
 771 cyclotron (EMIC) waves (e.g., Kitamura et al., 2021) and whistler-mode waves (Watt
 772 et al., 2011; Xia et al., 2016; X.-J. Zhang et al., 2019). This ULF wave coupling
 773 with EMIC and whistler-mode waves is the main mechanism responsible for quasi-
 774 periodic wave dynamics (W. Li et al., 2011; Xia et al., 2020; L. Li et al., 2022) that
 775 further controls quasi-periodic electron resonant scattering and subsequent precipitation-
 776 related loss (Artemyev et al., 2021; Bashir et al., 2022; Shi et al., 2022).

777 2. Other ULF wave modes and transients with a more broadband frequency spec-
 778 trum can have large amplitudes (e.g., Zhu & Kivelson, 1991; M. D. Hartinger, An-
 779 gelopoulos, et al., 2013) relative to normal modes and may dominate trends in sta-
 780 tistical analysis of band-integrated wave power. This is undesirable in studies seek-
 781 ing to determine how normal mode properties vary according to changing driv-
 782 ing conditions for the purpose of obtaining radial diffusion coefficients or, more
 783 broadly, for understanding the driving mechanisms of particular ULF wave modes.
 784 For example, Pc5 band-integrated compressional wave power - encompassing a range
 785 of phenomena such as drift-mirror waves, magnetopause surface waves, cavity/waveguide
 786 modes, transient increases/decreases in magnetic field - generally decreases with
 787 increasing distance from the magnetopause, but more narrowband wave activity
 788 associated with MHD normal modes does not necessarily follow this pattern, with
 789 local maxima occurring well inside the magnetopause (e.g., Figure 8).

790 Separating normal modes from other sources of ULF wave power would thus be advan-
 791 tageous for developing empirical models of ULF wave power needed to obtain radial dif-
 792 fusion coefficients. The results in this study and Takahashi and Anderson (1992) sug-
 793 gest that wave spectra with background trends removed, validated against numerical sim-
 794 ulations, are one tool for addressing this objective. However, more work is needed to de-
 795 termine how MHD normal mode wave power varies under different driving conditions
 796 and in different spatial regions, as has been done for ground and space observations of
 797 ULF wave power more broadly (e.g., Takahashi & Ukhorskiy, 2007; Bentley et al., 2018,
 798 2020).

799 5 Summary

800 We used ~ 13 years of THEMIS satellite magnetic field observations, combined with
 801 MHD numerical simulations, to examine the properties of MHD normal modes in the
 802 region $L > 5$ and for frequencies < 80 mHz, focusing on the dawn local time sector. We
 803 examine median wave power from detrended spectra as a function of spatial location (ra-
 804 dial distance, magnetic latitude), frequency, magnetopause location, and Alfvén speed
 805 profile peak (x_{ib}). Our findings are summarized as follows:

- 806 1. We identify persistent normal mode structure in observed power spectra with frequency-
 807 dependent wave power peaks like those obtained from ensemble simulation aver-
 808 ages, where the simulations assume different radial Alfvén speed profiles and mag-
 809 netopause locations. This is somewhat surprising given the known variability in
 810 the outer magnetosphere in radial Alfvén speed profile structure, variable driv-
 811 ing conditions, and the presence of other wave modes with larger amplitudes, all
 812 of which may have been expected to obscure or blur normal mode properties in
 813 median power spectra.
- 814 2. The properties of the normal modes, including rapid changes in frequency, are closely
 815 tied to the magnetopause location and radial Alfvén speed profile peaks.
- 816 3. Shifting the local Alfvén speed profile peak into the outer magnetosphere breaks
 817 the assumption of monotonically decaying Alfvén speed with increasing radial dis-
 818 tance that is assumed in most theory and modeling work. This changes several
 819 MHD normal mode properties: more compressional wave power trapped earth-
 820 ward of the Alfvén speed peak at Pc3-4 frequencies, less compressional wave power

- 821 able to penetrate the inner magnetosphere at Pc5 frequencies, non-monotonically
 822 varying Alfvén frequencies.
- 823 4. Persistent cavity/waveguide mode power peaks occur well inside the magnetopause
 824 and have frequencies that vary with magnetopause location.
 - 825 5. MHD normal modes do not always follow the same trends as seen in past ULF
 826 wave statistical studies examining band-integrated wave power, likely due in part
 827 to the presence of other wave modes (e.g., drift-mirror mode) or the averaging out
 828 of frequency-dependent normal mode structure.

829 In section 4 we discuss how these results could be used to improve radiation belt mod-
 830 els affected by isolating normal modes from other wave modes and transients prior to
 831 obtaining statistical wave power results and related radial diffusion coefficients. Future
 832 work should examine how MHD normal mode properties are affected in a wider range
 833 of internal and external driving conditions and at more locations. Additionally, more work
 834 is needed to compare these results to results obtained from ground-based radars and mag-
 835 netometers to better understand how normal modes are modified by ionospheric and ground
 836 conductance, thus improve ground-based remote sensing techniques and develop under-
 837 standing of other space weather impacts of normal modes such as geomagnetically in-
 838 duced currents (e.g., Heyns et al., 2021; M. D. Hartinger et al., 2023).

839 6 Open Research

840 The geomagnetic activity indices and solar wind parameters are publicly available
 841 at the NASA Space Science Data Facility (<https://omniweb.gsfc.nasa.gov/>). The
 842 THEMIS ULF wave database used to generate the data Figures in this manuscript is pub-
 843 licly available on the Zenodo repository (Hartinger, 2023), while the data used to gener-
 844 ate the simulation Figures are publicly available on the figshare repository (Elsden, 2023).
 845 All THEMIS data were accessed via the SPEDAS software and are publicly available at
 846 the THEMIS Berkeley data repository (<http://themis.ssl.berkeley.edu/index.shtml>).
 847 The SPEDAS software package used for processing the data can be obtained from the
 848 THEMIS website (<http://themis.ssl.berkeley.edu/index.shtml>). Wave power spec-
 849 tral densities were obtained using the publicly available “cross_spectrum” IDL software
 850 (https://github.com/svdataman/IDL/blob/master/src/cross_spectrum.pro).

851 Acknowledgments

852 MDH was supported by NASA 80NSSC19K0127, 80NSSC19K0907, 80NSSC21K1683,
 853 80NSSC21K1677, 80NSSC23K0903, and NSF AGS-2307204. KT was supported by NASA
 854 80NSSC19K0259 and 80NSSC21K0453. MOA was supported by a UKRI (STFC / EP-
 855 SRC) Stephen Hawking Fellowship EP/T01735X/1. The research of A.W. was funded
 856 in part by Science and Technology Facilities Council (STFC) grant ST/W001195/1 (UK).
 857 T.E. was funded in part by a Leverhulme Early Career Fellowship ECF-2019-155 (UK).
 858 AA and XZ were supported by NASA 80NSSC21K0729 and 80NSSC23K0108. We ac-
 859 knowledge support from ISSI Bern through ISSI International Team projects 483 “The
 860 Identification And Classification Of 3D Alfvén Resonances” and 546 “Magnetohydrody-
 861 namic Surface Waves at Earth’s Magnetosphere (and Beyond).” We acknowledge NASA
 862 contract NAS5-02099 and V. Angelopoulos for use of data from the THEMIS Mission.
 863 Specifically: C. W. Carlson and J. P. McFadden for use of ESA data; K. H. Glassmeier,
 864 U. Auster and W. Baumjohann for the use of FGM data provided under the lead of the
 865 Technical University of Braunschweig and with financial support through the German
 866 Ministry for Economy and Technology and the German Center for Aviation and Space
 867 (DLR) under contract 50 OC 0302. We thank the NASA Space Science Data facility for
 868 the use of solar wind data and geomagnetic activity indices.

869

References

- 870 Anderson, B. J., Engebretson, M. J., Rounds, S. P., Zanetti, L. J., & Potemra,
871 T. A. (1990, July). A statistical study of Pc 3-5 pulsations observed
872 by the AmMPTE/CCE magnetic fields experiment 1. Occurrence distri-
873 butions. *Journal of Geophysical Research*, *95*(A7), 10495-10523. doi:
874 10.1029/JA095iA07p10495
- 875 Angelopoulos, V. (2008, December). The THEMIS Mission. *Space Science Reviews*,
876 *141*(1-4), 5-34. doi: 10.1007/s11214-008-9336-1
- 877 Angelopoulos, V., Cruce, P., Drozdov, A., Grimes, E. W., Hatzigeorgiu, N., King,
878 D. A., ... Schroeder, P. (2019, January). The Space Physics Environment
879 Data Analysis System (SPEDAS). *Space Science Reviews*, *215*(1), 9. doi:
880 10.1007/s11214-018-0576-4
- 881 Archer, M. O., Hartinger, M. D., Walsh, B. M., & Angelopoulos, V. (2017, January).
882 Magnetospheric and solar wind dependences of coupled fast-mode resonances
883 outside the plasmasphere. *Journal of Geophysical Research (Space Physics)*,
884 *122*(1), 212-226. doi: 10.1002/2016JA023428
- 885 Archer, M. O., Hartinger, M. D., Walsh, B. M., Plaschke, F., & Angelopoulos, V.
886 (2015, December). Frequency variability of standing Alfvén waves excited
887 by fast mode resonances in the outer magnetosphere. *Geophysical Research*
888 *Letters*, *42*(23), 10,150-10,159. doi: 10.1002/2015GL066683
- 889 Artemyev, A. V., Demekhov, A. G., Zhang, X. J., Angelopoulos, V., Moure-
890 nas, D., Fedorenko, Y. V., ... Shinohara, I. (2021, November). Role of
891 Ducting in Relativistic Electron Loss by Whistler-Mode Wave Scattering.
892 *Journal of Geophysical Research (Space Physics)*, *126*(11), e29851. doi:
893 10.1029/2021JA029851
- 894 Auster, H. U., Glassmeier, K. H., Magnes, W., Aydogar, O., Baumjohann, W.,
895 Constantinescu, D., ... Wiedemann, M. (2008, December). The themis
896 fluxgate magnetometer. *Space Science Reviews*, *141*, 235-264. doi:
897 10.1007/s11214-008-9365-9
- 898 Bashir, M. F., Artemyev, A., Zhang, X.-J., & Angelopoulos, V. (2022, January). En-
899 ergetic Electron Precipitation Driven by the Combined Effect of ULF, EMIC,
900 and Whistler Waves. *Journal of Geophysical Research (Space Physics)*, *127*(1),
901 e29871. doi: 10.1029/2021JA029871
- 902 Bentley, S. N., Stout, J. R., Bloch, T. E., & Watt, C. E. J. (2020, October). Ran-
903 dom Forest Model of Ultralow-Frequency Magnetospheric Wave Power. *Earth*
904 *and Space Science*, *7*(10), e01274. doi: 10.1029/2020EA001274
- 905 Bentley, S. N., Watt, C. E. J., Owens, M. J., & Rae, I. J. (2018, April). ULF
906 Wave Activity in the Magnetosphere: Resolving Solar Wind Interdependen-
907 cies to Identify Driving Mechanisms. *Journal of Geophysical Research (Space*
908 *Physics)*, *123*(4), 2745-2771. doi: 10.1002/2017JA024740
- 909 Brautigam, D. H., Ginet, G. P., Albert, J. M., Wygant, J. R., Rowland, D. E., Ling,
910 A., & Bass, J. (2005, February). CRRES electric field power spectra and
911 radial diffusion coefficients. *Journal of Geophysical Research (Space Physics)*,
912 *110*(A2), A02214. doi: 10.1029/2004JA010612
- 913 Carpenter, D. L., & Anderson, R. R. (1992, February). An ISEE/Whistler Model of
914 Equatorial Electron Density in the Magnetosphere. *Journal of Geophysical Re-*
915 *search*, *97*(A2), 1097-1108. doi: 10.1029/91JA01548
- 916 Chi, P. J., & Russell, C. T. (1998, December). Phase skipping and Poynting flux
917 of continuous pulsations. *Journal of Geophysical Research*, *103*(A12), 29479-
918 29492. doi: 10.1029/98JA02101
- 919 Dai, L., Takahashi, K., Lysak, R., Wang, C., Wygant, J. R., Kletzing, C., ... Chen,
920 L. (2015, June). Storm time occurrence and spatial distribution of Pc4 poloidal
921 ULF waves in the inner magnetosphere: A Van Allen Probes statistical study.
922 *Journal of Geophysical Research (Space Physics)*, *120*(6), 4748-4762. doi:
923 10.1002/2015JA021134

- 924 Degeling, A. W., Rae, I. J., Watt, C. E. J., Shi, Q. Q., Rankin, R., & Zong, Q. G.
 925 (2018, February). Control of ULF Wave Accessibility to the Inner Magneto-
 926 sphere by the Convection of Plasma Density. *Journal of Geophysical Research*
 927 (*Space Physics*), *123*(2), 1086-1099. doi: 10.1002/2017JA024874
- 928 Degeling, A. W., & Rankin, R. (2008, Oct). Resonant drift echoes in electron phase
 929 space density produced by dayside Pc5 waves following a geomagnetic storm.
 930 *Journal of Geophysical Research (Space Physics)*, *113*(A10), A10220. doi:
 931 10.1029/2008JA013254
- 932 Degeling, A. W., Rankin, R., Kabin, K., Rae, I. J., & Fenrich, F. R. (2010,
 933 October). Modeling ULF waves in a compressed dipole magnetic field.
 934 *Journal of Geophysical Research (Space Physics)*, *115*, A10212. doi:
 935 10.1029/2010JA015410
- 936 Di Matteo, S., & Villante, U. (2018, March). The Identification of Waves at
 937 Discrete Frequencies at the Geostationary Orbit: The Role of the Data
 938 Analysis Techniques and the Comparison With Solar Wind Observations.
 939 *Journal of Geophysical Research (Space Physics)*, *123*(3), 1953-1968. doi:
 940 10.1002/2017JA024922
- 941 Di Matteo, S., Villante, U., Viall, N., Kepko, L., & Wallace, S. (2022, March). On
 942 Differentiating Multiple Types of ULF Magnetospheric Waves in Response
 943 to Solar Wind Periodic Density Structures. *Journal of Geophysical Research*
 944 (*Space Physics*), *127*(3), e30144. doi: 10.1029/2021JA030144
- 945 Drozdov, A. Y., Allison, H. J., Shprits, Y. Y., Elkington, S. R., & Aseev, N. A.
 946 (2021, August). A Comparison of Radial Diffusion Coefficients in 1-D and
 947 3-D Long-Term Radiation Belt Simulations. *Journal of Geophysical Research*
 948 (*Space Physics*), *126*(8), e28707. doi: 10.1029/2020JA028707
- 949 Elkington, S. R., Hudson, M. K., & Chan, A. A. (1999, Jan). Acceleration of
 950 relativistic electrons via drift-resonant interaction with toroidal-mode Pc-
 951 5 ULF oscillations. *Geophysical Research Letters*, *26*(21), 3273-3276. doi:
 952 10.1029/1999GL003659
- 953 Elkington, S. R., Hudson, M. K., & Chan, A. A. (2003, Mar). Resonant accel-
 954 eration and diffusion of outer zone electrons in an asymmetric geomagnetic
 955 field. *Journal of Geophysical Research (Space Physics)*, *108*(A3), 1116. doi:
 956 10.1029/2001JA009202
- 957 Elkington, S. R., & Sarris, T. E. (2016, 11). The Role of Pc-5 ULF Waves in the
 958 Radiation Belts: Current Understanding and Open Questions. In *Waves,*
 959 *Particles, and Storms in Geospace: A Complex Interplay*. Oxford Uni-
 960 versity Press. Retrieved from [https://doi.org/10.1093/acprof:oso/](https://doi.org/10.1093/acprof:oso/9780198705246.003.0005)
 961 [9780198705246.003.0005](https://doi.org/10.1093/acprof:oso/9780198705246.003.0005) doi: 10.1093/acprof:oso/9780198705246.003.0005
- 962 Elsdén, T. (2023). *Data for: 'properties of magnetohydrodynamic normal modes*
 963 *in the earth's magnetosphere', by hartinger et al., submitted to jgr space*
 964 *physics* [dataset]. figshare. Retrieved from [https://doi.org/10.6084/](https://doi.org/10.6084/m9.figshare.24433849.v1)
 965 [m9.figshare.24433849.v1](https://doi.org/10.6084/m9.figshare.24433849.v1) doi: 10.6084/m9.figshare.24433849.v1
- 966 Elsdén, T., Wright, A., & Degeling, A. (2022, September). A review of the theory of
 967 3-D Alfvén (field line) resonances. *Frontiers in Astronomy and Space Sciences*,
 968 *9*, 917817. doi: 10.3389/fspas.2022.917817
- 969 Elsdén, T., & Wright, A. N. (2019, January). The Effect of Fast Normal
 970 Mode Structure and Magnetopause Forcing on FLRs in a 3-D Waveguide.
 971 *Journal of Geophysical Research (Space Physics)*, *124*(1), 178-196. doi:
 972 10.1029/2018JA026222
- 973 Elsdén, T., & Wright, A. N. (2022, February). Polarization Properties of 3-D Field
 974 Line Resonances. *Journal of Geophysical Research (Space Physics)*, *127*(2),
 975 e30080. doi: 10.1029/2021JA030080
- 976 Fei, Y., Chan, A. A., Elkington, S. R., & Wiltberger, M. J. (2006, Dec). Radial dif-
 977 fusion and MHD particle simulations of relativistic electron transport by ULF
 978 waves in the September 1998 storm. *Journal of Geophysical Research (Space*

- 979 *Physics*), 111(A12), A12209. doi: 10.1029/2005JA011211
- 980 Hartinger, M. (2023). *Themis ulf power dataset* [dataset]. Zenodo. Retrieved from
 981 <https://zenodo.org/record/7971722> doi: 10.5281/zenodo.7971722
- 982 Hartinger, M., Angelopoulos, V., Moldwin, M. B., Nishimura, Y., Turner, D. L.,
 983 Glassmeier, K.-H., ... Stolle, C. (2012, June). Observations of a Pc5
 984 global (cavity/waveguide) mode outside the plasmasphere by THEMIS.
 985 *Journal of Geophysical Research (Space Physics)*, 117(A6), A06202. doi:
 986 10.1029/2011JA017266
- 987 Hartinger, M. D., Angelopoulos, V., Moldwin, M. B., Takahashi, K., & Clausen,
 988 L. B. N. (2013, February). Statistical study of global modes outside the plas-
 989 masphere. *Journal of Geophysical Research (Space Physics)*, 118(2), 804-822.
 990 doi: 10.1002/jgra.50140
- 991 Hartinger, M. D., Moldwin, M. B., Takahashi, K., Bonnell, J. W., & Angelopoulos,
 992 V. (2013, October). Survey of the ULF wave Poynting vector near the Earth's
 993 magnetic equatorial plane. *Journal of Geophysical Research (Space Physics)*,
 994 118(10), 6212-6227. doi: 10.1002/jgra.50591
- 995 Hartinger, M. D., Shi, X., Rodger, C. J., Fujii, I., Rigler, E. J., Kappler, K., ...
 996 Petersen, T. (2023, May). Determining ULF Wave Contributions to Geo-
 997 magnetically Induced Currents: The Important Role of Sampling Rate. *Space*
 998 *Weather*, 21(5), e2022SW003340. doi: 10.1029/2022SW003340
- 999 Heyns, M. J., Lotz, S. I., & Gaunt, C. T. (2021, February). Geomagnetic Pul-
 1000 sations Driving Geomagnetically Induced Currents. *Space Weather*, 19(2),
 1001 e2020SW002557. doi: 10.1029/2020SW002557
- 1002 Hughes, W. J., Southwood, D. J., Mauk, B., McPherron, R. L., & Barfield, J. N.
 1003 (1978, September). Alfvén waves generated by an inverted plasma energy
 1004 distribution. *Nature*, 275, 43-45. doi: 10.1038/275043a0
- 1005 Jacobs, J. A., Kato, Y., Matsushita, S., & Troitskaya, V. A. (1964). Classification
 1006 of geomagnetic micropulsations. *Journal of Geophysical Research*, 69, 180-181.
 1007 doi: 10.1029/JZ069i001p00180
- 1008 Kitamura, N., Shoji, M., Nakamura, S., Kitahara, M., Amano, T., Omura, Y., ...
 1009 Burch, J. L. (2021, May). Energy Transfer Between Hot Protons and Elec-
 1010 tromagnetic Ion Cyclotron Waves in Compressional Pc5 Ultra low Frequency
 1011 Waves. *Journal of Geophysical Research (Space Physics)*, 126(5), e28912. doi:
 1012 10.1029/2020JA028912
- 1013 Kivelson, M. G., & Southwood, D. J. (1985, January). Resonant ULF waves: A
 1014 new interpretation. *Geophysical Research Letters*, 12(1), 49-52. doi: 10.1029/
 1015 GL012i001p00049
- 1016 Kivelson, M. G., & Southwood, D. J. (1986, April). Coupling of global magneto-
 1017 spheric MHD eigenmodes to field line resonances. *Journal of Geophysical Re-*
 1018 *search*, 91(A4), 4345-4351. doi: 10.1029/JA091iA04p04345
- 1019 Laakso, H., & Pedersen, A. (1998, January). Ambient Electron Density Derived
 1020 from Differential Potential Measurements. *Geophysical Monograph Series*, 102,
 1021 49. doi: 10.1029/GM102p0049
- 1022 Lee, D.-H., & Kim, K. (1999, June). Compressional MHD waves in the magne-
 1023 tosphere: A new approach. *Journal of Geophysical Research*, 104(A6), 12379-
 1024 12386. doi: 10.1029/1999JA900053
- 1025 Lee, D.-H., & Lysak, R. L. (1989, December). Magnetospheric ULF wave coupling
 1026 in the dipole model: the impulsive excitation. *Journal of Geophysical Research*,
 1027 94(A12), 17097-17103. doi: 10.1029/JA094iA12p17097
- 1028 Lee, D.-H., & Lysak, R. L. (1990, January). Effects of azimuthal asymmetry on ULF
 1029 waves in the dipole magnetosphere. *Geophysical Research Letters*, 17(1), 53-56.
 1030 doi: 10.1029/GL017i001p00053
- 1031 Lee, D.-H., & Takahashi, K. (2006, January). MHD Eigenmodes in the Inner Magne-
 1032 tosphere. In *Magnetospheric ulf waves: Synthesis and new directions* (Vol. 169,
 1033 p. 73). doi: 10.1029/169GM07

- 1034 Lejosne, S., & Kollmann, P. (2020, February). Radiation Belt Radial Diffusion at
 1035 Earth and Beyond. *Space Science Reviews*, *216*(1), 19. doi: 10.1007/s11214
 1036 -020-0642-6
- 1037 Lessard, M. R., Hudson, M. K., & Lühr, H. (1999, March). A statistical study
 1038 of Pc3-Pc5 magnetic pulsations observed by the AMPTE/Ion Release Mod-
 1039 ule satellite. *Journal of Geophysical Research*, *104*(A3), 4523-4538. doi:
 1040 10.1029/1998JA900116
- 1041 Li, L., Omura, Y., Zhou, X.-Z., Zong, Q.-G., Rankin, R., Yue, C., & Fu, S.-Y.
 1042 (2022, May). Nonlinear Wave Growth Analysis of Chorus Emissions Mod-
 1043 ulated by ULF Waves. *Geophysical Research Letters*, *49*(10), e97978. doi:
 1044 10.1029/2022GL097978
- 1045 Li, W., Thorne, R. M., Bortnik, J., Nishimura, Y., & Angelopoulos, V. (2011, June).
 1046 Modulation of whistler mode chorus waves: 1. Role of compressional Pc4-5
 1047 pulsations. *Journal of Geophysical Research (Space Physics)*, *116*, A06205.
 1048 doi: 10.1029/2010JA016312
- 1049 Mann, I. R., Chisham, G., & Bale, S. D. (1998, March). Multisatellite and ground-
 1050 based observations of a tailward propagating Pc5 magnetospheric wave-
 1051 guide mode. *Journal of Geophysical Research*, *103*(A3), 4657-4670. doi:
 1052 10.1029/97JA03175
- 1053 Matzka, J., Stolle, C., Yamazaki, Y., Bronkalla, O., & Morschhauser, A. (2021,
 1054 May). The Geomagnetic Kp Index and Derived Indices of Geomagnetic Activ-
 1055 ity. *Space Weather*, *19*(5), e2020SW002641. doi: 10.1029/2020SW002641
- 1056 McFadden, J. P., Carlson, C. W., Larson, D., Bonnell, J., Mozer, F., Angelopoulos,
 1057 V., ... Auster, U. (2008, December). THEMIS ESA First Science Results
 1058 and Performance Issues. *Space Science Reviews*, *141*(1-4), 477-508. doi:
 1059 10.1007/s11214-008-9433-1
- 1060 McFadden, J. P., Carlson, C. W., Larson, D., Ludlam, M., Abiad, R., Elliott, B., ...
 1061 Angelopoulos, V. (2008, December). The THEMIS ESA Plasma Instrument
 1062 and In-flight Calibration. *Space Science Reviews*, *141*(1-4), 277-302. doi:
 1063 10.1007/s11214-008-9440-2
- 1064 Moore, T. E., Gallagher, D. L., Horwitz, J. L., & Comfort, R. H. (1987, October).
 1065 MHD wave breaking in the outer plasmasphere. *Geophysical Research Letters*,
 1066 *14*(10), 1007-1010. doi: 10.1029/GL014i010p01007
- 1067 Murphy, K. R., Mann, I. R., & Sibeck, D. G. (2015, Nov). On the dependence
 1068 of storm time ULF wave power on magnetopause location: Impacts for ULF
 1069 wave radial diffusion. *Geophysical Research Letters*, *42*(22), 9676-9684. doi:
 1070 10.1002/2015GL066592
- 1071 O'Brien, T. P., & Moldwin, M. B. (2003, February). Empirical plasmopause mod-
 1072 els from magnetic indices. *Geophysical Research Letters*, *30*(4), 1152. doi: 10
 1073 .1029/2002GL016007
- 1074 Ozeke, L. G., Mann, I. R., Murphy, K. R., Jonathan Rae, I., & Milling, D. K. (2014,
 1075 March). Analytic expressions for ULF wave radiation belt radial diffusion co-
 1076 efficients. *Journal of Geophysical Research (Space Physics)*, *119*(3), 1587-1605.
 1077 doi: 10.1002/2013JA019204
- 1078 Plaschke, F., & Glassmeier, K. H. (2011, October). Properties of standing Kruskal-
 1079 Schwarzschild-modes at the magnetopause. *Annales Geophysicae*, *29*(10),
 1080 1793-1807. doi: 10.5194/angeo-29-1793-2011
- 1081 Rae, I. J., Mann, I. R., Watt, C. E. J., Kistler, L. M., & Baumjohann, W. (2007,
 1082 November). Equator-S observations of drift mirror mode waves in the dawnside
 1083 magnetosphere. *Journal of Geophysical Research (Space Physics)*, *112*(A11),
 1084 A11203. doi: 10.1029/2006JA012064
- 1085 Samson, J. C., Harrold, B. G., Ruohoniemi, J. M., Greenwald, R. A., & Walker,
 1086 A. D. M. (1992, March). Field line resonances associated with MHD wave-
 1087 guides in the magnetosphere. *Geophysical Research Letters*, *19*(5), 441-444. doi:
 1088 10.1029/92GL00116

- 1089 Sandhu, J. K., Rae, I. J., Staples, F. A., Hartley, D. P., Walach, M. T., Elsden, T.,
1090 & Murphy, K. R. (2021, July). The Roles of the Magnetopause and Plasma-
1091 pause in Storm-Time ULF Wave Power Enhancements. *Journal of Geophysical*
1092 *Research (Space Physics)*, *126*(7), e29337. doi: 10.1029/2021JA029337
- 1093 Sandhu, J. K., Rae, I. J., Wygant, J. R., Breneman, A. W., Tian, S., Watt, C. E. J.,
1094 ... Walach, M. T. (2021, April). ULF Wave Driven Radial Diffusion During
1095 Geomagnetic Storms: A Statistical Analysis of Van Allen Probes Observa-
1096 tions. *Journal of Geophysical Research (Space Physics)*, *126*(4), e29024. doi:
1097 10.1029/2020JA029024
- 1098 Sarris, T. E., Li, X., Zhao, H., Papadakis, K., Liu, W., Tu, W., ... Imajo, S. (2022,
1099 October). Distribution of ULF Wave Power in Magnetic Latitude and Local
1100 Time Using THEMIS and Arase Measurements. *Journal of Geophysical Re-*
1101 *search (Space Physics)*, *127*(10), e2022JA030469. doi: 10.1029/2022JA030469
- 1102 Shi, X., Baker, J. B. H., Ruohoniemi, J. M., Hartinger, M. D., Frissell, N. A., & Liu,
1103 J. (2017, April). Simultaneous space and ground-based observations of a plas-
1104 maspheric virtual resonance. *Journal of Geophysical Research (Space Physics)*,
1105 *122*(4), 4190-4209. doi: 10.1002/2016JA023583
- 1106 Shi, X., Zhang, X.-J., Artemyev, A., Angelopoulos, V., Hartinger, M. D., Tsai,
1107 E., & Wilkins, C. (2022, December). On the Role of ULF Waves in the
1108 Spatial and Temporal Periodicity of Energetic Electron Precipitation. *Jour-*
1109 *nal of Geophysical Research (Space Physics)*, *127*(12), e2022JA030932. doi:
1110 10.1029/2022JA030932
- 1111 Shue, J. H., Chao, J. K., Fu, H. C., Russell, C. T., Song, P., Khurana, K. K., &
1112 Singer, H. J. (1997, May). A new functional form to study the solar wind
1113 control of the magnetopause size and shape. *Journal of Geophysical Research*,
1114 *102*(A5), 9497-9512. doi: 10.1029/97JA00196
- 1115 Southwood, D. J. (1974, March). Some features of field line resonances in the mag-
1116 netosphere. *Planetary and Space Science*, *22*(3), 483-491. doi: 10.1016/0032
1117 -0633(74)90078-6
- 1118 Southwood, D. J., & Hughes, W. J. (1983, August). Theory of hydromagnetic waves
1119 in the magnetosphere. *Space Science Reviews*, *35*(4), 301-366. doi: 10.1007/
1120 BF00169231
- 1121 Sugiura, M., & Wilson, C. R. (1964). Oscillation of the Geomagnetic Field Lines and
1122 Associated Magnetic Perturbations at Conjugate Points. *Journal of Geophysi-*
1123 *cal Research*, *69*(7), 1211-1216. doi: 10.1029/JZ069i007p01211
- 1124 Takahashi, K., & Anderson, B. J. (1992, July). Distribution of ULF energy ($f_i=80$
1125 mHz) in the inner magnetosphere: A statistical analysis of AMPTE CCE mag-
1126 netic field data. *Journal of Geophysical Research*, *97*(A7), 10751-10773. doi:
1127 10.1029/92JA00328
- 1128 Takahashi, K., Bonnell, J., Glassmeier, K.-H., Angelopoulos, V., Singer, H. J., Chi,
1129 P. J., ... Liu, W. (2010, December). Multipoint observation of fast mode
1130 waves trapped in the dayside plasmasphere. *Journal of Geophysical Research*
1131 *(Space Physics)*, *115*(A12), A12247. doi: 10.1029/2010JA015956
- 1132 Takahashi, K., Hartinger, M. D., Angelopoulos, V., & Glassmeier, K.-H. (2015, Au-
1133 gust). A statistical study of fundamental toroidal mode standing Alfvén waves
1134 using THEMIS ion bulk velocity data. *Journal of Geophysical Research (Space*
1135 *Physics)*, *120*(8), 6474-6495. doi: 10.1002/2015JA021207
- 1136 Takahashi, K., McPherron, R. L., & Terasawa, T. (1984, May). Dependence of the
1137 spectrum of Pc 3-4 pulsations on the interplanetary magnetic field. *Journal of*
1138 *Geophysical Research*, *89*(A5), 2770-2780. doi: 10.1029/JA089iA05p02770
- 1139 Takahashi, K., & Ukhorskiy, A. Y. (2007, Nov). Solar wind control of Pc5 pul-
1140 sation power at geosynchronous orbit. *Journal of Geophysical Research (Space*
1141 *Physics)*, *112*(A11), A11205. doi: 10.1029/2007JA012483
- 1142 Tamao, T. (1965). Transmission and coupling resonance of hydromagnetic distur-
1143 bances in the non-uniform Earth's magnetosphere. *Science reports of the To-*

- 1144 *hoku University. Series 5, Geophysics, 17*, 43–70.
- 1145 Watt, C. E. J., Degeling, A. W., Rankin, R., Murphy, K. R., Rae, I. J., & Singer,
1146 H. J. (2011, October). Ultralow-frequency modulation of whistler-mode wave
1147 growth. *Journal of Geophysical Research (Space Physics)*, *116*(A10), A10209.
1148 doi: 10.1029/2011JA016730
- 1149 Wharton, S. J., Wright, D. M., Yeoman, T. K., James, M. K., & Sandhu, J. K.
1150 (2019, July). The Variation of Resonating Magnetospheric Field Lines With
1151 Changing Geomagnetic and Solar Wind Conditions. *Journal of Geophysical
1152 Research (Space Physics)*, *124*(7), 5353-5375. doi: 10.1029/2019JA026848
- 1153 Wright, A. N., & Elsdén, T. (2020, February). Simulations of MHD Wave Propa-
1154 gation and Coupling in a 3-D Magnetosphere. *Journal of Geophysical Research
1155 (Space Physics)*, *125*(2), e27589. doi: 10.1029/2019JA027589
- 1156 Wright, A. N., & Mann, I. R. (2006, January). Global MHD Eigenmodes of the
1157 Outer Magnetosphere. In *Magnetospheric ulf waves: Synthesis and new direc-
1158 tions* (Vol. 169, p. 51). doi: 10.1029/169GM06
- 1159 Xia, Z., Chen, L., Dai, L., Claudepierre, S. G., Chan, A. A., Soto-Chavez, A. R.,
1160 & Reeves, G. D. (2016, September). Modulation of chorus intensity by ULF
1161 waves deep in the inner magnetosphere. *Geophysical Research Letters*, *43*,
1162 9444-9452. doi: 10.1002/2016GL070280
- 1163 Xia, Z., Chen, L., & Li, W. (2020, November). Statistical Study of Chorus Mod-
1164 ulations by Background Magnetic Field and Plasma Density. *Geophysical Re-
1165 search Letters*, *47*(22), e89344. doi: 10.1029/2020GL089344
- 1166 Zhang, D., Liu, W., Zhang, Z., Li, X., Sarris, T. E., Goldstein, J., & Dmitry, R.
1167 (2023, March). Cavity Mode Wave Frequency Variation Associated With In-
1168 ward Motion of the Magnetopause During Interplanetary Shock Compression.
1169 *Journal of Geophysical Research (Space Physics)*, *128*(3), e2023JA031299. doi:
1170 10.1029/2023JA031299
- 1171 Zhang, X. J., Angelopoulos, V., Artemyev, A. V., Hartinger, M. D., & Bortnik, J.
1172 (2020, October). Modulation of Whistler Waves by Ultra-Low-Frequency Per-
1173 turbations: The Importance of Magnetopause Location. *Journal of Geophysical
1174 Research (Space Physics)*, *125*(10), e28334. doi: 10.1029/2020JA028334
- 1175 Zhang, X.-J., Chen, L., Artemyev, A. V., Angelopoulos, V., & Liu, X. (2019,
1176 November). Periodic Excitation of Chorus and ECH Waves Modulated by
1177 Ultralow Frequency Compressions. *Journal of Geophysical Research (Space
1178 Physics)*, *124*(11), 8535-8550. doi: 10.1029/2019JA027201
- 1179 Zhu, X., & Kivelson, M. G. (1991, November). Compressional ULF waves in the
1180 outer magnetosphere 1. Statistical study. *Journal of Geophysical Research*,
1181 *96*(A11), 19451-19467. doi: 10.1029/91JA01860
- 1182 Zong, Q., Rankin, R., & Zhou, X. (2017). The interaction of ultra-low-frequency
1183 pc3-5 waves with charged particles in earth's magnetosphere. *Reviews of Mod-
1184 ern Plasma Physics*, *1*, 10. doi: 10.1007/s41614-017-0011-4